https://doi.org/10.5194/egusphere-2025-626
Preprint. Discussion started: 20 May 2025
© Author(s) 2025. CC BY 4.0 License.

# Measurement Report: Unraveling $PM_{10}$ Sources and Oxidative Potential Across Chinese Regions: Insights Analysis Based on CNN-LSTM and Receptor Model

Qinghe Cai[1], Dongqing Fang[2,3], Junli Jin[3], Xiaoyu Hu[4], Yuxuan Cao[1], Tianyi Zhao[1,5], Yang Bai[1], Yang Zhang[1,6]

[1]College of Resources and Environment, University of Chinese Academy of Sciences, Beijing, 100049, China
[2]Key Laboratory of Urban Meteorology, China Meteorological Administration, Beijing 100089, China
[3]Meteorological Observation Center, China Meteorological Administration, Beijing, 100081, China
[4]City University of Hong Kong, Hongkong, 999077, China
[5]Guangzhou Institute of Geochemistry, Chinese Academy of Sciences, Guangzhou, 510640, China
[6]Beijing Yanshan Earth Critical Zone National Research Station, Beijing, 101408, China

*Correspondence to*: Dongqing Fang (fangdongqing@163.com) and Yang Zhang (zhangyang@ucas.ac.cn)

**Abstract.** The oxidative potential (OP) of particulate matter is a key driver of $PM_{10}$-induced adverse health effects, triggering oxidative stress and inflammatory responses that increase respiratory and cardiovascular disease risks. To evaluate $PM_{10}$ and its OP characteristics across China, samples were collected from twelve representative monitoring stations from June 2022 to May 2023. A deep learning model combining Convolutional Neural Networks and Long Short-Term Memory networks (CNN-LSTM) was employed to reconstruct anomalous $PM_{10}$ data, achieving $R^2$ values of 0.967 and 0.884 for training and test sets, respectively. Significant spatial variations in $PM_{10}$ were observed, with highest concentrations in the northwestern regions (Xi'an: 98.20 ± 52.92 $\mu g \cdot m^{-3}$, Dunhuang: 90.36 ± 54.72 $\mu g \cdot m^{-3}$), the lowest in the northeast (Longfengshan: 40.04 ± 24.04 $\mu g \cdot m^{-3}$, Dalian: 40.35 ± 15.66 $\mu g \cdot m^{-3}$), and elevated levels in suburban areas (average: 85.43 ± 46.69 $\mu g \cdot m^{-3}$). Urban sites showed the highest OP values, with significantly higher $PM_{10}$ concentrations in northern regions compared to southern ones ($p<0.05$). Most sites exhibited peak $PM_{10}$ and OP levels in winter and lowest in summer. Source apportionment using Positive Matrix Factorization (PMF) revealed dust (13.2-27.4%), biomass burning (9.5-39.3%), traffic (16.6-21.4%), and agricultural activities (13-22%) as main contributors to $PM_{10}$. PMF analysis identified traffic as the primary OP contributor (24-48%) across sites, with regional variations in biomass burning (57% in Nanning), agricultural activities (37% in Zhengzhou), and dust (22-23% in Gucheng and Longfengshan). These findings highlight the need to control traffic emissions and other major sources to reduce OP and protect public health.

## 1 Introduction

Particulate matter (PM) is one of the main pollutants affecting air quality and human health. Among these, $PM_{10}$, which refers to suspended particles with an aerodynamic diameter of 10 μm or less, has received considerable attention due to its complex sources, extensive environmental and health effects. The sources of $PM_{10}$ are both complex and diverse, including anthropogenic activities such as fossil fuel combustion, industrial production, traffic emissions and dust, as well as natural

https://doi.org/10.5194/egusphere-2025-626
Preprint. Discussion started: 20 May 2025
© Author(s) 2025. CC BY 4.0 License.

sources such as dust storms and volcanic eruptions (Xue et al., 2010). Due to its small particle size, $PM_{10}$ can remain suspended in the atmosphere for extended periods of time, significantly affecting atmospheric visibility while potentially exerting profound effects on regional and global climate change through both direct and indirect mechanisms (Shao et al., 2000). More critically, $PM_{10}$ poses a serious threat to human health. Upon entering the human body via the respiratory system, it can be deposited in the airways and lungs, triggering respiratory diseases such as asthma, chronic obstructive pulmonary disease (COPD) and even lung cancer (Cao et al., 2016). Furthermore, $PM_{10}$ can penetrate the alveolar barrier and enter the circulatory system, inducing systemic diseases such as cardiovascular disease and diabetes (Huang, 2023).

In the context of accelerating global industrialization and urbanization, $PM_{10}$ pollution has emerged as a critical environmental concern. Research conducted by the World Health Organization (WHO) indicates that air pollution is responsible for millions of premature deaths worldwide each year, with $PM_{10}$ being a major contributor (Cohen et al., 2005). The mechanisms by which $PM_{10}$ affects human health are diverse and complex, one of the primary mechanisms being its ability to induce excessive production of reactive oxygen species (ROS), subsequently triggering oxidative stress (OS) effects. Components within $PM_{10}$, such as transition metals and polycyclic aromatic hydrocarbons (PAHs), can directly or indirectly promote ROS generation, leading to cell membrane lipid peroxidation, protein denaturation, and DNA damage (Chirino et al., 2010). Furthermore, ROS can activate inflammatory signaling pathways, including nuclear factor κB (NF-κB), which amplify inflammatory responses and further leading to cellular dysfunction and tissue damage(Wang et al., 2017). This interplay between oxidative stress and inflammatory responses is considered a critical pathophysiological basis for various $PM_{10}$-induced diseases. Several studies suggest that OP may be a more accurate indicator of PM health effects than its mass concentration, providing a new perspective for assessing PM health risks(Gao et al., 2020; Bates et al., 2019) .

The oxidative potential (OP) of particulate matter (PM) serves as a critical indicator for assessing its toxicity and is closely related to the generation of reactive oxygen species (ROS). Research indicates that the OP of PM is strongly correlated with its physicochemical properties and sources(He and Zhang, 2023). In particular, PM of smaller size typically exhibits higher OP, possibly due to its larger specific surface area and enhanced bioavailability (Saffari et al., 2014; Yao et al., 2024). Water-soluble transition metals (e.g., iron and copper) and organic carbon (e.g., PAHs) in PM are considered to be the primary chemical components that influence OP. These components can induce ROS generation either by catalyzing Fenton reactions or by directly participating in redox processes (Saffari et al., 2014; Guo et al., 2020). Sources of OP in PM are varied and include primarily traffic emissions, fossil fuel combustion, and secondary organic aerosol formation (Bates et al., 2019; Saffari et al., 2014). Upon entering the human body, PM from these sources can potentially induce oxidative stress, impair cellular antioxidant defenses, and lead to lipid peroxidation, protein denaturation, and DNA damage, thereby triggering a range of health problems (Ghio et al., 2012). Significantly, photochemical aging of PM in the atmosphere further enhances its OP, possibly related to the formation of secondary organic aerosols and changes in oxidation states of metallic components during the aging process (An et al., 2022). In addition, the oxygen content in the fuel has been shown to be a critical factor affecting OP, as exemplified by the typically high OP of PM generated from biomass combustion (Hedayat et al., 2016).

https://doi.org/10.5194/egusphere-2025-626
Preprint. Discussion started: 20 May 2025
© Author(s) 2025. CC BY 4.0 License.

However, an accurate assessment of the health risks associated with $PM_{10}$ requires an accurate analysis of its sources and chemical compositions. Due to the complex origins of $PM_{10}$ and the significant temporal variations in its chemical compositions, traditional source attribution methods often face challenges when processing large-scale, high-dimensional environmental data. In recent years, with the rapid development of deep learning technology, its application in handling environmental data anomalies has received increasing attention. Deep learning models, particularly the combination of Convolutional Neural Networks (CNN) and Long Short-Term Memory networks (LSTM), have demonstrated significant advantages in handling anomalies within time series data. CNNs effectively extract spatial features, while LSTMs excel at capturing long-term dependencies in time series (Huang and Kuo, 2018; Li et al., 2020). This hybrid model not only identifies anomalies, but also improves data completeness and reliability by predicting and replacing anomalous values(Lee et al., 2019; Qin et al., 2019). Compared with traditional machine learning methods, CNN-LSTM models show superior performance in several evaluation metrics, such as MAE and RMSE (Huang and Kuo, 2018; Yang et al., 2020a; Li et al., 2020). CNN-LSTM models retain significant value in processing atmospheric particulate matter data even without time series analysis. Their spatial feature extraction capabilities effectively identify and correct anomalies caused by instrument malfunction or local pollution events, thereby improving data quality (Zhang and Zhou, 2023). Through training and learning, CNN-LSTM models can effectively predict and correct anomalous values, providing a high-quality data foundation for subsequent analysis(Li et al., 2020; Yang et al., 2020a).

After data pre-processing, the Positive Matrix Factorization (PMF) model was used to analyse $PM_{10}$ sources in this study. The PMF model can identify major pollution sources and their contribution rates by decomposing the observation data matrix without requiring prior information (Paatero and Tapper, 1994). In recent years, PMF models have been extensively applied in $PM_{10}$ and $PM_{2.5}$ source apportionment, often in combination with other techniques such as multiple linear regression (MLR) (Weber et al., 2018) . Based on the source contribution results from PMF analysis, MLR models can further quantify the contributions of different sources to the OP of PM, providing crucial evidence to reveal the association between PM sources and their health effects. Recent studies have innovatively introduced machine learning methods, such as multilayer perceptron (MLP), to model OP based on source contribution results from PMF analysis, significantly improving model predictive accuracy and explanatory power (Borlaza et al., 2022).

In this study, we adopted a comprehensive approach to process $PM_{10}$ data and evaluate its OP. First, we removed anomalies from $PM_{10}$ data and used a deep learning model combining CNN and LSTM to predict and replace anomalous values. This method effectively captures spatial and temporal features in time-series data, thereby improving data completeness and prediction accuracy. Then, we employed the PMF model for $PM_{10}$ source apportionment to identify its major sources. Finally, we used the MLR model to quantitatively evaluate the contribution of different sources to OP. Through this series of methods, this study aims to reveal the OP characteristics and sources of $PM_{10}$ in typical regions of China.

https://doi.org/10.5194/egusphere-2025-626
Preprint. Discussion started: 20 May 2025
© Author(s) 2025. CC BY 4.0 License.

## 2 Materials and Methods

### 2.1 Sample Collections

Daliy ambient $PM_{10}$ samples were collected every three days from June 2022 to May 2023 at the twelve stations of the CMA Atmosphere Watch Network (CAWNET), with their distribution shown in **Figure 1** and detailed information provided in **Table 1.** Remote sites were selected in areas far from anthropogenic pollution sources to ensure the representativeness of the background monitoring data. Rural sites were selected in typical areas, with sampling points located away from local pollution sources and elevated above the surrounding ground to minimize local disturbances. At urban sites, sampling points were typically located 50-100 m above the average urban elevation in order to collect mixed aerosol samples rather than aerosols from single sources. Suburban sites were located in transition zones between urban and rural areas to reflect aerosol characteristics under different environmental conditions. All aerosol samples were collected using MiniVol$^{TM}$ air samplers (Airmetrics, Oregon, USA) operating continuously for 24 hours from 9:00 AM to 9:00 AM the following day (Beijing time) at a flow rate of 5 L·min$^{-1}$. Whatman 47 mm quartz fiber filters (QM/A) were used for sampling. To prevent contamination from affecting the experimental results, all filters were heated at 800°C for 3 hours prior to use to remove potential organic contaminants.

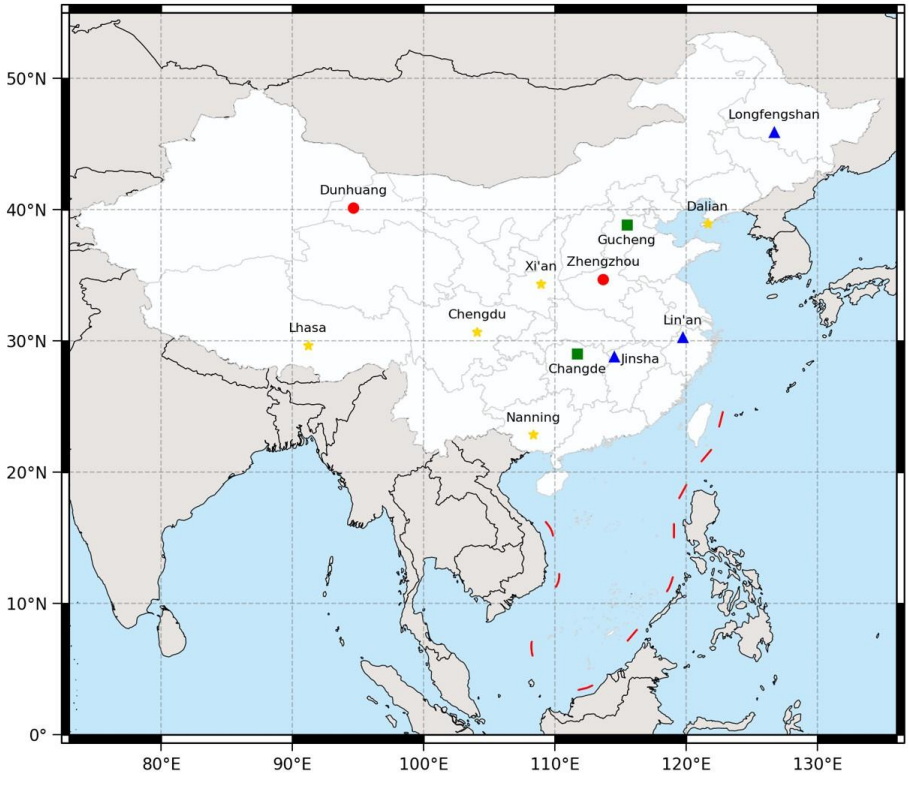


**Figure 1. Locations of 12 CAWNET stations. The map base is from the Ministry of Natural Resources' Standard Map Service, review number GS(2019)1822.**

https://doi.org/10.5194/egusphere-2025-626
Preprint. Discussion started: 20 May 2025
© Author(s) 2025. CC BY 4.0 License.

**Table 1. Information for twelve CAWNET stations.**

| Station name | Province | Lat.&Long. | Elev.(m) | Type |
|---|---|---|---|---|
| Changde (CHD) | Hunan | 29° 10.2' N, 111° 42.6' E | 150.6 | Rural |
| Chengdu (CD) | Sichuan | 30° 39 'N, 104° 2.4' E | 587.0 | Urban |
| Dalian (DL) | Liaoning | 38° 54' N, 121° 37.8' E | 91.5 | Urban |
| Dunhuang (DH) | Gansu | 40° 9' N, 94° 40.8' E | 1137.5 | Suburban |
| Gucheng (GC) | Hebei | 39° 7.8' N, 115° 48' E | 15.2 | Rural |
| Jinsha (JS) | Hubei | 29° 37.8' N, 114° 12' E | 751.4 | Remote |
| Lhasa (LS) | Tibet | 29° 40.2' N, 91° 7.8' E | 3660.0 | Urban |
| Lin'an(LA) | Zhejiang | 30° 18' N, 119° 44' E | 138.6 | Remote |
| Longfengshan (LFS) | Heilongjiang | 44° 43.8' N, 127° 36' E | 331.0 | Remote |
| Nanning (NN) | Guangxi | 22° 49.2' N, 108° 21' E | 159.0 | Urban |
| Xi'an (XA) | Shaanxi | 34° 25.8' N, 108° 58.2' E | 363.0 | Urban |
| Zhengzhou (ZZ) | Henan | 34° 46.8' N, 113° 40.8' E | 110.4 | Suburban |

## 2.2 Chemical and OP analysis

### 2.2.1 Chemical compositions analysis

Quantitative measurements of OC and EC were performed using the DRI Model 2015A thermal/optical carbon analyzer developed by the Desert Research Institute, USA. After OC and EC analysis, ion chromatography (Dionex 600 series, USA) was used to analyze and determine various ions, including $Na^+$, $NH_4^+$, $K^+$, $Ca^{2+}$, $Mg^{2+}$, $F^-$, $Cl^-$, $NO_3^-$, and $SO_4^{2-}$. This method has been widely used as a highly efficient and sensitive analytical technique for the determination of water-soluble ions in $PM_{10}$ and $PM_{2.5}$ (Domingos et al., 2012; Cui et al., 2008; Yan et al., 2006).

### 2.2.2 Oxidative Potential (OP) analysis

The 2',7'-Dichlorodihydrofluorescein (DCFH) method is widely used for detecting particle-bound ROS, mainly due to its lack of specificity and selectivity for various ROS species(Antonini et al., 1998; Cohn et al., 2008; Huang et al., 2016). In this study, the 2',7'-Dichlorodihydrofluorescein diacetate (DCFH-DA) probe method was employed to measure ROS levels induced by $PM_{10}$. First, DCFH-DA (97%, Sigma-Aldrich, USA) was prepared as a 1 mmol mL-1 stock solution using anhydrous ethanol and mixed with 0.01 mol $L^{-1}$ NaOH solution in a 1:4 (v/v) ratio. The mixture was kept at room temperature in the dark for 30 min to ensure complete alkaline hydrolysis of DCFH-DA to DCFH. Phosphate buffer solution (PBS, 0.0067 mol $L^{-1}$, pH 7.2) was then added to adjust the pH to 7.0-7.4. The hydrolyzed DCFH solution was stored at 4°C in the dark and used within 2 hours. Horseradish peroxidase (HRP) was dissolved in phosphate buffer to prepare a 10 unit·$mL^{-1}$ HRP stock solution. It was mixed with the DCFH solution prior to use to achieve final concentrations of 10 μmol·$L^{-1}$ DCFH and 0.5 units·$mL^{-1}$ HRP in

https://doi.org/10.5194/egusphere-2025-626
Preprint. Discussion started: 20 May 2025
© Author(s) 2025. CC BY 4.0 License.

the reaction system. To generate a standard curve, a 1000 μg·mL$^{-1}$ $H_2O_2$ solution was diluted with ultrapure water to generate $H_2O_2$ standard solutions at concentrations of 20, 40, 80, 160, 200, 240, 320, 400, and 800 nmol·L$^{-1}$. In a 96-well plate, 20 μL standard solution and 60 μL DCFH-HRP mixture were added, with three replicates for each concentration. After 15 minutes of dark incubation at 37°C, fluorescence intensity was measured using a multifunctional microplate reader (SynergyTMH1, BioTek America) at an excitation wavelength of 485 nm and an emission wavelength of 535 nm. Quantification was done through converting the sample's fluorescent intensity to the equivalent quantity of $H_2O_2$ (nmol $H_2O_2$·m$^{-3}$). Before sample analysis, $PM_{10}$ samples were extracted in phosphate buffer solution by sonication for 30 minutes. After centrifugation, the supernatant was collected for testing. In the 96-well plate, 20 μL of sample solution and 60 μL of DCFH-HRP mixture were added, with three replicates per sample. Water blanks, filter blanks, and DCFH-HRP background blanks were included to eliminate background interference. After 15 minutes of dark incubation at 37°C, fluorescence intensity was measured and converted to $H_2O_2$ equivalent concentrations using the $H_2O_2$ standard curve to characterize $PM_{10}$-induced ROS levels. Throughout the experimental procedure, the microplate reader was preheated for 30 minutes before measurement to ensure a stable incubation temperature of 37°C. Background fluorescence values were subtracted from each measurement, and the relative standard deviation (RSD) of the replicates was controlled within 5% to ensure the accuracy and reliability of the data.

### 2.3 Data analysis

#### 2.3.1 Convolutional Neural Network（CNN）

One-dimensional convolutional neural networks (1D-CNN) have significant theoretical advantages and practical value in processing time series data. The core mechanism relies on local connectivity and weight sharing, where each neuron is connected only to a local region of the input data, while the convolution kernel weights are shared across the entire input sequence. This design significantly reduces the number of model parameters, improving computational efficiency while effectively mitigating overfitting problems. Moreover, 1D-CNN achieves translational invariance through convolution and pooling operations, ensuring robustness to input data translations and enabling stable capture of key patterns in time-series data. Crucially, 1D-CNN possesses automatic feature extraction capabilities, allowing the model to independently learn and extract multi-level feature representations from raw data through end-to-end training, thus reducing dependence on manual feature engineering. As illustrated in **Figure 2**, the input sequence $x_1$~ $x_6$ undergoes convolution operations to generate feature mappings $y_1$ ~ $y_4$, with purple, green, and yellow connections linking the input layer to the convolution layer. Each connection maintains its distinct weight value, with connections of the same color sharing identical weights. By stacking multiple convolutional layers, the model progressively learns higher-level feature representations, offering robust expressive capabilities for time-series data modeling and prediction.

https://doi.org/10.5194/egusphere-2025-626
Preprint. Discussion started: 20 May 2025
© Author(s) 2025. CC BY 4.0 License.

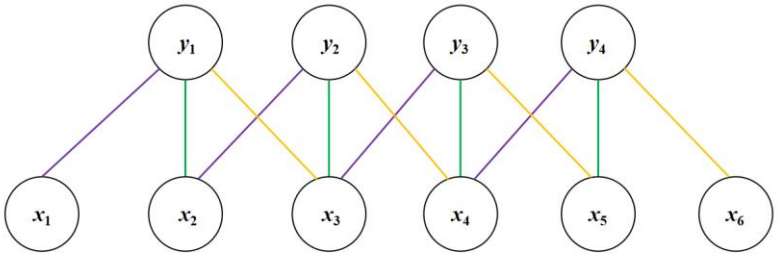


**Figure 2. The one-dimensional (1D) convolution operation process.**

### 2.3.2 Long Short-Term Memory（LSTM）

Long Short-Term Memory (LSTM) networks are specialized recurrent neural networks that effectively address the long-term dependency problems inherent in traditional RNN(Hochreiter and Schmidhuber, 1997). LSTM introduces memory cells and gating mechanisms that selectively remember or forget information, enabling the capture of long-term dependencies in sequences (Okut, 2021). The network uses three primary gating mechanisms: the forgetting gate, the input gate, and the output gate. The operating principle of the LSTM is illustrated in **Figure 3,** where σ represents the sigmoid function as shown in Eq. (1). Compared to traditional RNNs, LSTM networks exhibit superior handling of the vanishing gradient problem and can learn dependencies over longer time steps (Sherstinsky, 2020). These capabilities have led to the widespread application of LSTM in various domains, including time series prediction and natural language processing (Vennerød et al., 2021). The specific mathematical formulations of LSTM are detailed in Eqs. (1) - (6):

$$f_t = \sigma\left(W_f \cdot [h_{t-1}, x_t] + b_f\right) \quad (1)$$

$$i_t = \sigma(W_i \cdot [h_{t-1}, x_t] + b_i) \quad (2)$$

$$\tilde{c}_t = tanh(W_c \cdot [h_{t-1}, x_t] + b_c) \quad (3)$$

$$c_t = f_t \times c_{t-1} + i_t \times \tilde{c}_t \quad (4)$$

$$o_t = \sigma(W_o \cdot [h_{t-1}, x_t] + b_o) \quad (5)$$

$$h_t = o_t \times tanh(c_t) \quad (6)$$

Where $W_f$ represents the weight matrix of the forget gate, and $b_f$ denotes its bias term. $h_{t-1}$ is the previous hidden state and $x_t$ is the current input. The sigmoid activation function $\sigma$ controls the proportion of information retention. $i_t$ represents the output of the input gate, while $\tilde{c}_t$ indicates the candidate memory value. $W_i$ and $W_c$ represent the weight matrices for the input gate and candidate memory respectively, while $b_i$ and $b_c$ denote their corresponding bias terms. $c_t$ represents the memory cell state at the current time step. $W_o$ denotes the weight matrix of the output gate, $b_o$ represents its bias term, and $o_t$ indicates the output of the output gate.

https://doi.org/10.5194/egusphere-2025-626
Preprint. Discussion started: 20 May 2025
© Author(s) 2025. CC BY 4.0 License.

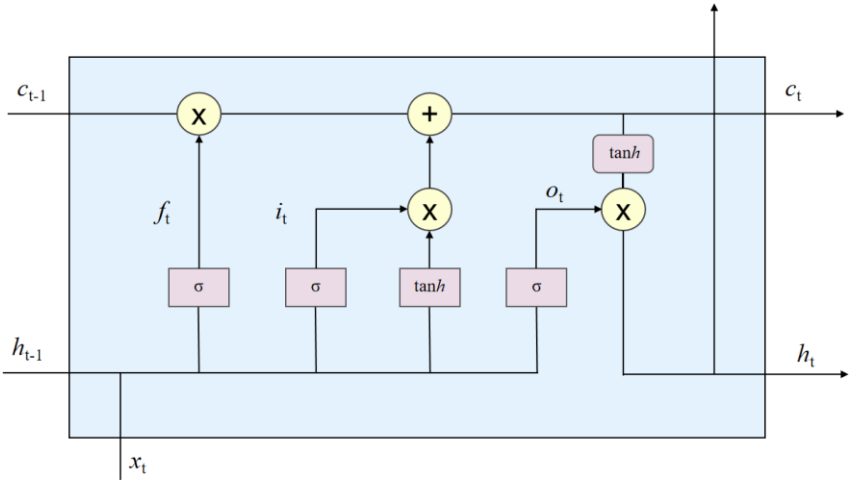


**Figure 3. The schematic diagram of the Long Short-Term Memory (LSTM).**

### 2.3.3 CNN-LSTM Network Model

Several studies have shown that CNN-LSTM models have excellent performance in PM prediction, with low error rates and reduced training times (Li et al., 2020; Huang and Kuo, 2018). In this study, $PM_{10}$ concentration data were preprocessed for 11 chemical components: OM, EC, $Na^+$, $NH_4^+$, $K^+$, $Ca^{2+}$, $Mg^{2+}$, $F^-$, $Cl^-$, $NO_3^-$, and $SO_4^{2-}$. Specifically, if the sum of the chemical components in a data set exceeded the $PM_{10}$ mass concentration or fell below 50% of the $PM_{10}$ mass concentration, the $PM_{10}$ concentration in that data set was considered anomalous and removed. After screening, the remaining data were retained and included in the training set. A hybrid model combining Convolutional Neural Networks (CNN) and Long Short-Term Memory (LSTM) was used to predict $PM_{10}$ concentrations based on the training set. The model first extracts local features from the data through two CNN layers: the first CNN layer uses 16 channels and a kernel size of 2, while the second CNN layer uses 32 channels and the same kernel size, capturing local feature patterns through a sliding window with a stride of 1. Each CNN layer is followed by a ReLU activation function to introduce non-linearity, and a Dropout layer with a probability of 0.2 to enhance generalization capability. Subsequently, a 2-layer LSTM network (with 64 hidden units) captures long-term dependencies in the time series, with the LSTM layers also applying the same Dropout mechanism; finally, the prediction results are output through a fully connected layer. During the training process, Mean Squared Error (MSE) was used as the loss function, and the Adam optimizer was employed for parameter optimization, with an initial learning rate set to 0.0005. When training the model, a total of 3000 training epochs were set, while dynamically monitoring the loss value, with early stopping when the loss value fell below a preset threshold of 0.0007. Upon completion of training, the model was evaluated on both training and test sets by calculating Mean Absolute Error (MAE), Root Mean Square Error (RMSE), and Coefficient of Determination ($R^2$) to comprehensively evaluate the predictive performance of the model.

https://doi.org/10.5194/egusphere-2025-626
Preprint. Discussion started: 20 May 2025
© Author(s) 2025. CC BY 4.0 License.

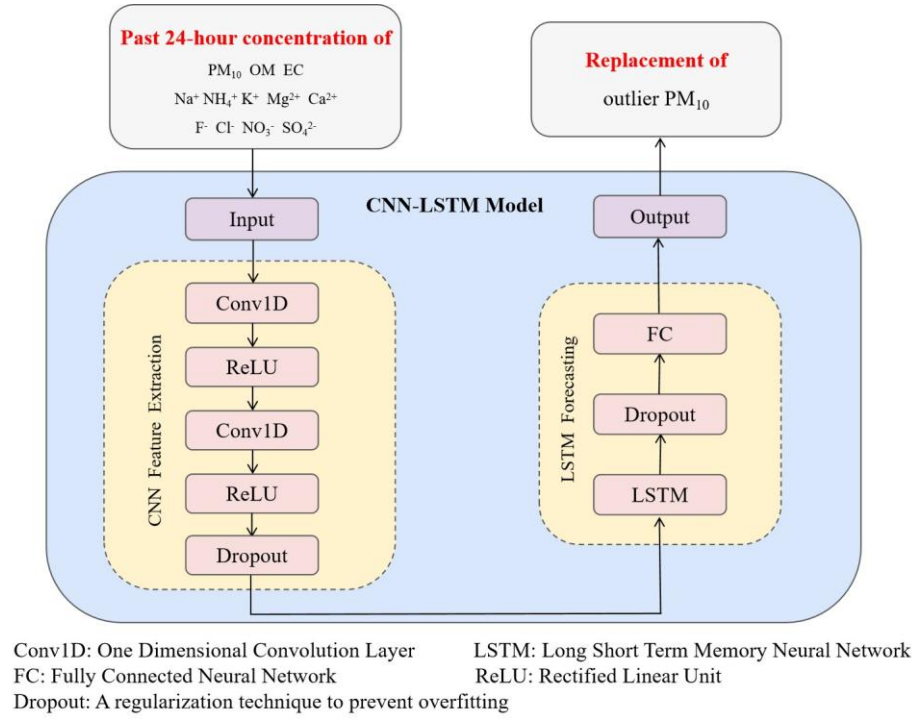


**Figure 4. The architecture of the CNN-LSTM in this study.**

### 2.4 Source apportionment

#### 2.4.1 PM mass apportionment: positive matrix factorization（PMF）

In this study, the US Environmental Protection Agency (US-EPA) EPA PMF 5.0 software (US-EPA, 2017) was used to perform source apportionment of $PM_{10}$. Positive matrix factorization (PMF) is a multivariate statistical method based on factor analysis that has been widely applied in source apportionment studies of atmospheric particulate matter (Paatero and Tapper, 1994). The PMF model identifies pollution sources and their contribution rates by decomposing the observed data matrix into two non-negative matrices - the factor contribution matrix (G) and the factor profile matrix (F). The mathematical model can be expressed as:

$$X = GF + E \tag{7}$$

Where $X$ is the observation data matrix (n×m), $G$ is the factor contribution matrix (n×p), $F$ is the factor profile matrix (p×m), and $E$ is the residual matrix. The PMF model optimizes the decomposition results by minimizing the objective function $Q$:

$$Q = \sum_{i=1}^{n}\sum_{j=1}^{m}\left(\frac{x_{ij} - \sum_{k=1}^{p} g_{ik}f_{kj}}{u_{ij}}\right) \tag{8}$$

Where $x_{ij}$ is the concentration of chemical component $j$ in sample $i$, $u_{ij}$ is the corresponding uncertainty, $g_{ik}$ is the contribution of factor $k$ in sample $i$, and $f_{kj}$ is the proportion of chemical component $j$ in factor $k$. By introducing non-negative

https://doi.org/10.5194/egusphere-2025-626
Preprint. Discussion started: 20 May 2025
© Author(s) 2025. CC BY 4.0 License.

constraints, the PMF model can more reasonably explain the physical significance of pollution sources (Paatero, 1997). The uncertainty ($Unc$) of the sample data is calculated using Eqs. (9) and (10):

$$Unc = \frac{5}{6} \times MDL(x_{ij} < MDL) \quad (9)$$

$$Unc = \sqrt{(EF_{ij} \times x_{ij})^2 + (0.5 \times MDL)^2}(x_{ij} \geq MDL) \quad (10)$$

Where $MDL$ represents the method detection limit, and $EF_{ij}$ denotes the error fraction of component *j* in sample *i*. In this study, the $EF$ values for $OP_v$ were set as the standard deviation during analysis (Verma et al., 2015), while the other components were set at 10%.

## 3 Results and discussion

### 3.1 CNN-LSTM prediction results

The CNN-LSTM model includes input data consisting of $PM_{10}$ concentration measurements and eleven chemical constituents, including OM (1.4*OC), EC, $Na^+$, $NH_4^+$, $K^+$, $Ca^{2+}$, $Mg^{2+}$, $F^-$, $Cl^-$, $NO_3^-$, and $SO_4^{2-}$. To ensure the integrity of the data quality, outlier elimination was performed based on the sum of the chemical components. Specifically, data points were classified as outliers and subsequently removed if the sum of the components exceeded the $PM_{10}$ concentration or fell below 50% of the $PM_{10}$ concentration. After this screening process, 471 datasets were retained for model training and evaluation, with 85% allocated to the training set and 15% to the test set. In addition, 766 datasets identified as outliers were excluded and subjected to prediction. Model performance was evaluated independently on both the training and test sets using three metrics: Mean Absolute Error (MAE), Root Mean Square Error (RMSE), and Coefficient of Determination ($R^2$). These performance metrics are mathematically expressed in Eqs. (11) - (13). In these equations,$y_i$ represents the actual value, $\hat{y}_i$ denotes the predicted value, n indicates the sample size, and $\overline{y}$ represents the mean of the actual values.

$$MAE = \frac{1}{n}\sum_{i=1}^{n}|y_i - \hat{y}_i| \quad (11)$$

$$RMSE = \sqrt{\frac{1}{n}\sum_{i=1}^{n}(y_i - \hat{y}_i)^2} \quad (12)$$

$$R^2 = 1 - \frac{\sum_{i=1}^{n}(y_i - \hat{y}_i)^2}{\sum_{i=1}^{n}(y_i - \overline{y})^2} \quad (13)$$

The model was evaluated on both the training and test sets after completion of training, with results presented in **Table 2** and **Figure 5.** For the training set, the model achieved a mean absolute error (MAE) of 6.6614 $\mu g \cdot m^{-3}$, a root mean square error (RMSE) of 8.7162 $\mu g \cdot m^{-3}$, and a coefficient of determination ($R^2$) of 0.9670. W When evaluated on the test set, the model demonstrated an MAE of 12.6705 $\mu g \cdot m^{-3}$, a RMSE of 17.4965 $\mu g \cdot m^{-3}$, and an $R^2$ of 0.8840. These performance metrics indicate

https://doi.org/10.5194/egusphere-2025-626
Preprint. Discussion started: 20 May 2025
© Author(s) 2025. CC BY 4.0 License.

that the CNN-LSTM architecture has a robust ability to learn the characteristics of atmospheric particulate matter composition, effectively capturing the complex relationships between $PM_{10}$ concentrations and their chemical constituents.

**Table 2. CNN-LSTM model prediction accuracy.**

| Data | MAE（μg·m$^{-3}$） | RMSE（μg·m$^{-3}$） | $R^2$ |
|---|---|---|---|
| Train | 6.61 | 8.72 | 0.9670 |
| Test | 12.67 | 17.50 | 0.8840 |

**Figure 5 (a)** illustrates the temporal evolution of the loss values for training sets. The plots show a progressive decrease in loss values for training datasets as training progresses, eventually converging below the predetermined threshold of 0.0007. This convergence pattern indicates satisfactory model training with no apparent overfitting problems. **Figure 5 (b) and (c)** show the comparative analysis between predicted and observed values across training and test sets. The results show strong agreement between model predictions and actual measurements, with particularly high prediction accuracy observed in regions of lower $PM_{10}$ concentrations. However, slight deviations occur in regions with higher $PM_{10}$ concentrations. This reduced performance at higher concentrations may be due to the limited number of high concentration samples in the dataset, potentially limiting the ability of the model to accurately fit extreme values (Liang et al., 2020).

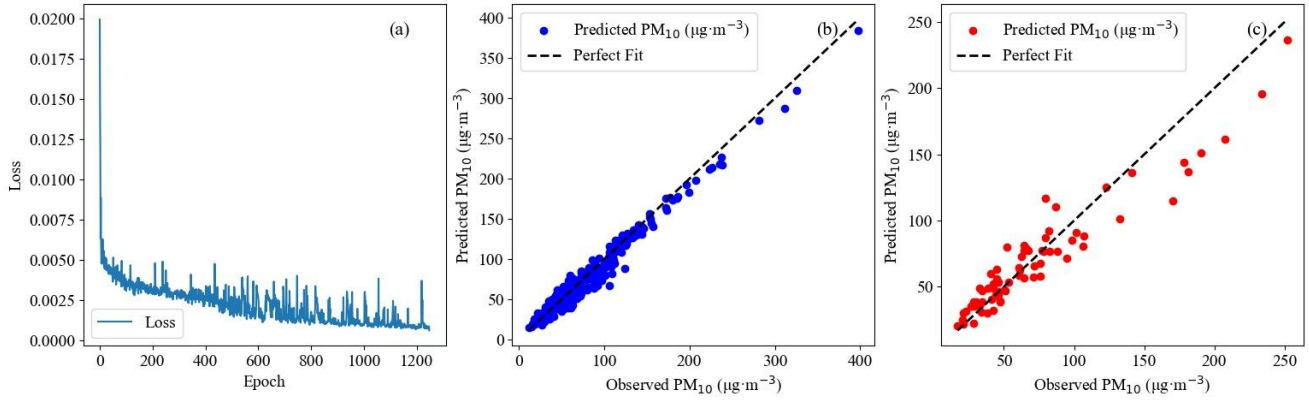


**Figure 5.(a) LOSS trends for the training sets; comparison of predictions and observations for the (b) training and (c) test sets by the CNN-LSTM mode.**

### 3.2 $PM_{10}$ mass and chemical composition concentrations

#### 3.2.1 Annual average

The analysis of $PM_{10}$ concentrations across diverse locations in China shows a remarkable spatial variation in the annual mean concentrations of $PM_{10}$ and its chemical constituents from June 2022 to May 2023, as shown in **Table 3**. Significantly elevated $PM_{10}$ levels were observed at northwestern sites, with Xi'an and Dunhuang recording concentrations of 98.20 μg·m$^{-3}$ and 90.36 μg·m$^{-3}$, respectively, while other sites had concentrations ranging from 40 to 80 μg·m$^{-3}$. These spatial patterns suggest complex interactions between natural and anthropogenic factors. The elevated $PM_{10}$ concentrations observed in Xi'an, a major industrial

https://doi.org/10.5194/egusphere-2025-626
Preprint. Discussion started: 20 May 2025
© Author(s) 2025. CC BY 4.0 License.

city and densely populated metropolitan area, are primarily due to industrial emissions and substantial high traffic volumes. Due to located in an arid region, Dunhuang is likely influenced by dust storm events, as evidenced by higher concentrations of crustal elements such as $Ca^{2+}$ (Yu et al., 2020). While $Na^{+}$ is typically associated with sea salt spray, its presence at inland sites such as Dunhuang may indicate contributions from crustal material or other local sources(Zhang et al., 2014b).

In contrast, the lowest $PM_{10}$ concentrations were observed at Longfengshan (LFS) and Dalian (DL) in the northeastern region, with values of 40.04 $\mu g \cdot m^{-3}$ and 40.35 $\mu g \cdot m^{-3}$, respectively. These relatively lower concentrations may be due to relatively less anthropogenic activities and better air quality in these regions. Longfengshan, located at the interface of agricultural and forested landscapes, primarily receives $PM_{10}$ contributions from natural sources, such as soil dust resuspension and biomass burning reported in previous research (Yu et al., 2012). Meanwhile, Dalian's coastal location likely contributes to its lower $PM_{10}$ concentrations. The observed $Na^{+}$ concentration of 2.36 $\mu g \cdot m^{-3}$ in Dalian may reflect the influence of marine aerosols (Shi et al., 2022). In addition, air quality in Dalian is likely modulated by meteorological conditions, especially sea breezes, which facilitate the dispersion and dilution of pollutants, thereby reducing $PM_{10}$ concentrations(Wang et al., 2002).

In the densely populated regions of Gucheng (GC) and Zhengzhou (ZZ), where anthropogenic pollution sources are abundant, the annual mean $PM_{10}$ concentrations were 79.18 $\mu g \cdot m^{-3}$ and 80.50 $\mu g \cdot m^{-3}$, respectively. These elevated $PM_{10}$ levels are strongly correlated with intensive anthropogenic sources in these regions, including industrial activities, traffic emissions, and construction dust. As major industrial and transportation hubs, Gucheng and Zhengzhou have particularly high concentrations of organic matter (OM) and elemental carbon (EC), specifically 19.67 $\mu g \cdot m^{-3}$ and 4.89 $\mu g \cdot m^{-3}$ in Gucheng, 17.35 $\mu g\text{-}m^{-3}$ and 4.12 $\mu g \cdot m^{-3}$ in Zhengzhou. Additionally, the concentrations of sulfate ($SO_4^{2-}$) and nitrate ($NO_3^{-}$) concentrations in Zhengzhou and Gucheng were measured to be 8.70 $\mu g \cdot m^{-3}$, 13.71 $\mu g \cdot m^{-3}$ and 6.00 $\mu g \cdot m^{-3}$, 10.94 $\mu g \cdot m^{-3}$, respectively. These values, which are significantly higher than in other regions, indicate particularly active secondary aerosol formation processes in these areas(Yang et al., 2020b).

In the southwestern region, Chengdu (CD), located in the Sichuan Basin, recorded an annual mean $PM_{10}$ concentration of 59.56 $\mu g \cdot m^{-3}$. This region is characterized by high aerosol optical depth and reduced visibility, attributed to poor dispersion conditions and significant local industrial emissions (Li et al., 2003; Zhang et al., 2012).

The central Chinese sites of Jinsha (JS), Changde (CHD), and Lin'an (LA) showed relatively lower annual mean concentrations of $PM_{10}$ which are 47.17 $\mu g \cdot m^{-3}$, 46.59 $\mu g \cdot m^{-3}$, and 48.16 $\mu g \cdot m^{-3}$, respectively. Despite these lower concentrations, the chemical composition shows distinct regional characteristics. $Ca^{2+}$ concentrations of 2.48 $\mu g \cdot m^{-3}$ and 2.19 $\mu g \cdot m^{-3}$ in Jinsha and Lin'an, respectively, likely reflect contributions from soil dust resuspension (Shen, 2016). $K^{+}$ concentration of 0.44 $\mu g \cdot m^{-3}$ observed in Changde may be related to agricultural activities in the region (Liu et al., 2016).

Lhasa (LS), located in the center of the Tibetan Plateau at an elevation of 3,663 meters, has $PM_{10}$ concentrations that are primarily influenced by natural factors due to its relatively sparse population and limited industrial emissions. Nevertheless, Lhasa maintained an average $PM_{10}$ concentration of 47.82 $\mu g \cdot m^{-3}$, mainly due to extensive dust resuspension from arid and exposed terrain, coupled with regional dust storm events. The plateau's climatic conditions, characterized by particularly strong

https://doi.org/10.5194/egusphere-2025-626
Preprint. Discussion started: 20 May 2025
© Author(s) 2025. CC BY 4.0 License.

winds and low humidity, enhance the dispersal of soil dust and maintain relatively high $PM_{10}$ levels despite the absence of significant anthropogenic sources.

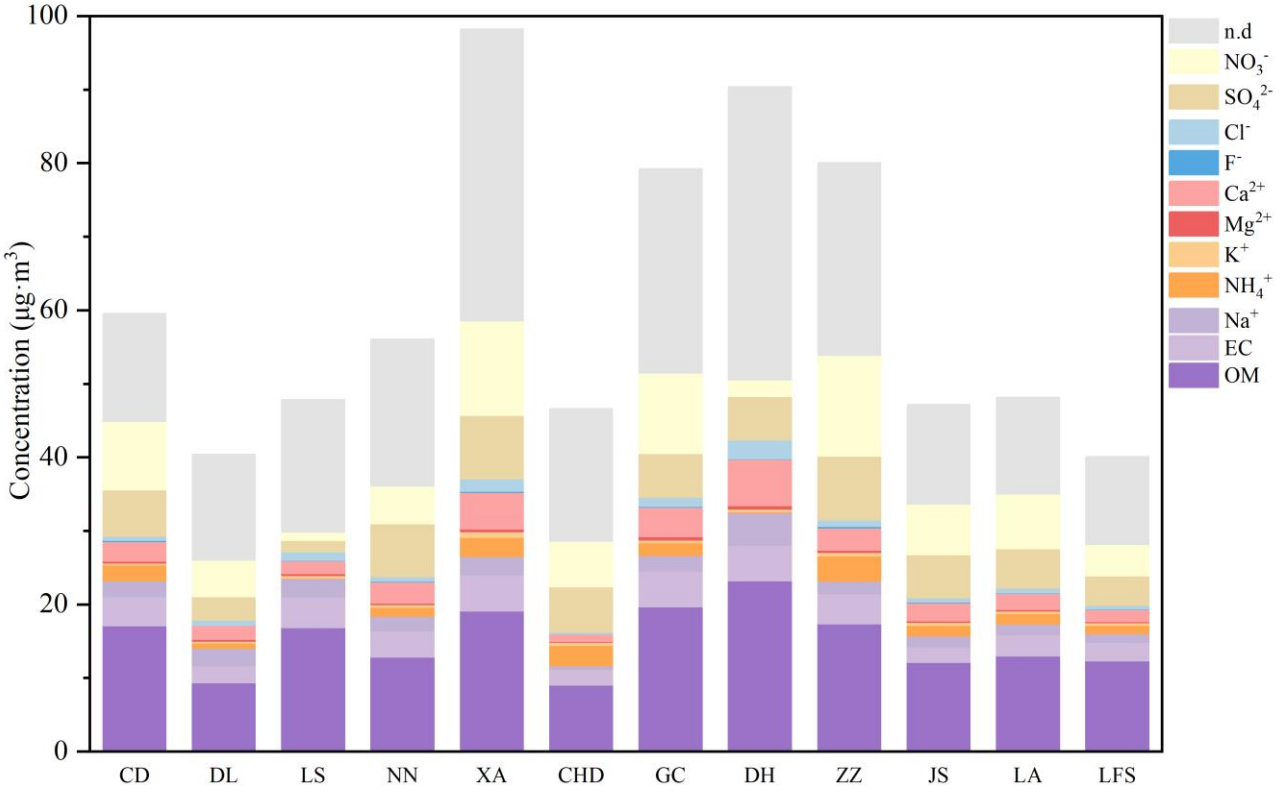


**Figure 6. Stacked representation of annual average $PM_{10}$ concentrations and chemical composition（μg $m^{-3}$） across Chinese regions, including unknown components, from June 2022 to May 2023. (n.d.: unknown components)**

The annual mean $PM_{10}$ concentrations for urban, rural, suburban, and remote sites were 59.99 μg·$m^{-3}$, 62.88 μg·$m^{-3}$, 85.43 μg·$m^{-3}$, and 45.12 μg·$m^{-3}$, respectively. These data show that urban-rural transition zones had the highest $PM_{10}$ concentrations, which may be due to the simultaneous influence of multiple pollution sources from both urban and rural areas, including industrial emissions, traffic pollution, and agricultural activities (Li et al., 2014). In contrast, background sites had the lowest $PM_{10}$ concentrations, reflecting minimal anthropogenic influence in these regions, with primary pollution sources consisting of natural dust resuspension and long-range transported pollutants (Jiao et al., 2021).

https://doi.org/10.5194/egusphere-2025-626
Preprint. Discussion started: 20 May 2025
© Author(s) 2025. CC BY 4.0 License.

**Table 3. Annual average concentrations (μg·m$^{-3}$) of $PM_{10}$ and its chemical composition in different regions of China from June 2022 to May 2023.**

| Station | Type | $PM_{10}$ | OM | EC | $Na^+$ | $NH_4^+$ | $K^+$ | $Mg^{2+}$ | $Ca^{2+}$ | $F^-$ | $Cl^-$ | $SO_4^{2-}$ | $NO_3^-$ |
|---|---|---|---|---|---|---|---|---|---|---|---|---|---|
| Chengdu | Urban | 59.56 | 17.09 | 3.97 | 2.18 | 2.11 | 0.30 | 0.23 | 2.67 | 0.15 | 0.58 | 6.29 | 9.36 |
| Dalian | Urban | 40.35 | 9.35 | 2.30 | 2.36 | 0.74 | 0.25 | 0.25 | 1.89 | 0.04 | 0.69 | 3.19 | 5.00 |
| Lhasa | Urban | 47.82 | 16.85 | 4.16 | 2.51 | 0.07 | 0.32 | 0.26 | 1.75 | 0.05 | 1.18 | 1.55 | 1.12 |
| Nanning | Urban | 54.23 | 12.87 | 3.50 | 2.03 | 1.20 | 0.37 | 0.21 | 2.89 | 0.07 | 0.64 | 7.21 | 5.09 |
| Xi'an | Urban | 98.20 | 19.13 | 4.87 | 2.50 | 2.64 | 0.76 | 0.37 | 4.97 | 0.15 | 1.67 | 8.67 | 12.82 |
| Changde | Rural | 46.59 | 9.05 | 2.17 | 0.44 | 2.76 | 0.44 | 0.08 | 1.02 | 0.03 | 0.27 | 6.16 | 6.18 |
| Gucheng | Rural | 79.18 | 19.67 | 4.89 | 2.08 | 1.78 | 0.35 | 0.46 | 4.01 | 0.09 | 1.21 | 6.00 | 10.94 |
| Dunhuang | Suburban | 90.36 | 23.24 | 4.78 | 4.43 | 0.16 | 0.36 | 0.46 | 6.31 | 0.06 | 2.57 | 5.90 | 2.29 |
| Zhengzhou | Suburban | 80.50 | 17.35 | 4.12 | 1.71 | 3.43 | 0.45 | 0.32 | 3.03 | 0.21 | 0.86 | 8.70 | 13.71 |
| Jinsha | Remote | 47.17 | 12.14 | 2.07 | 1.52 | 1.45 | 0.40 | 0.20 | 2.48 | 0.08 | 0.58 | 5.82 | 6.89 |
| Lin'an | Remote | 48.16 | 13.02 | 2.92 | 1.37 | 1.46 | 0.34 | 0.22 | 2.19 | 0.04 | 0.66 | 5.37 | 7.42 |
| Longfengshan | Remote | 40.04 | 12.31 | 2.52 | 1.21 | 1.14 | 0.36 | 0.15 | 1.61 | 0.06 | 0.50 | 4.04 | 4.25 |

https://doi.org/10.5194/egusphere-2025-626
Preprint. Discussion started: 20 May 2025
© Author(s) 2025. CC BY 4.0 License.

### 3.2.2 Seasonal variation

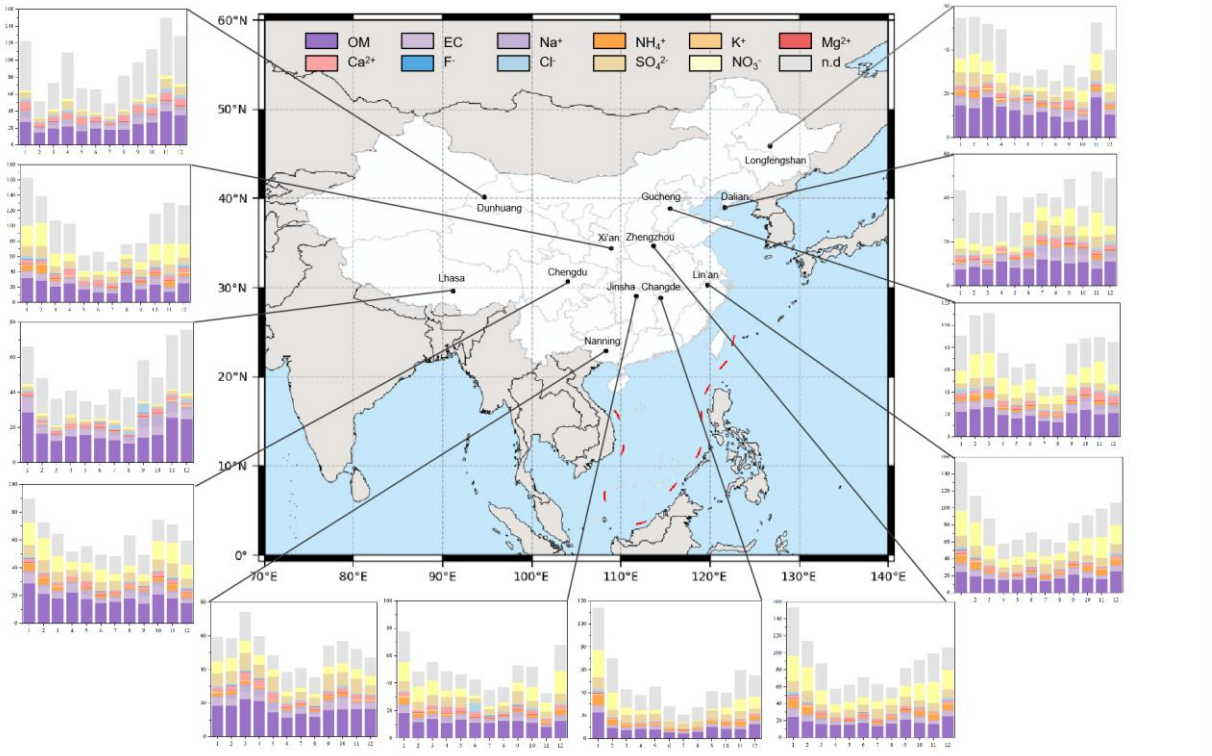


**Figure 7. Stacked Representation of Monthly averaged $PM_{10}$ Concentrations and Chemical Composition（$\mu g \cdot m^{-3}$）across Chinese Regions, Including Unknown Components from June 2022 to May 2023. (n.d: Unknown Components). The map base is from the Ministry of Natural Resources' Standard Map Service, review number GS(2019)1822.**

Seasonal variations in $PM_{10}$ concentrations are shown in **Figure 7**. Overall, the study area shows a significant seasonal differentiation of $PM_{10}$ concentrations, characterized by minimum levels in summer (June-August), maximum levels in winter (December-February), and a secondary peak in spring (March-May). Multiple studies have also identified distinct seasonal patterns in $PM_{10}$ concentrations, with minimal concentrations in summer and maximal concentrations in winter(Yang, 2009; Qu et al., 2010; Li et al., 2009). The lower $PM_{10}$ concentrations observed in summer may be attributed to increased precipitation, which effectively scavenges atmospheric particulate matter (Yang, 2009). In addition, research has shown significant negative correlations between $PM_{10}$ concentrations and temperature, as well as positive correlations with atmospheric pressure (Han et al., 2015; Li et al., 2019). Elevated $PM_{10}$ concentrations in winter are primarily associated with increased solid fuel consumption during the heating season (Tsvetanova et al., 2017). Additionally, unfavorable meteorological conditions in winter, including high atmospheric stability, reduced atmospheric boundary layer height, and frequent temperature inversions, exacerbate the accumulation of pollutants (Zhao et al., 2014). All six monitoring stations in the study area showed pronounced concentration peaks during the spring, which can be attributed to several factors. Firstly, the frequent occurrence of dust events

https://doi.org/10.5194/egusphere-2025-626
Preprint. Discussion started: 20 May 2025
© Author(s) 2025. CC BY 4.0 License.

during spring increases atmospheric particulate matter concentrations. Secondly, weak wind conditions and local circulation patterns establish local emissions as the primary source of $PM_{10}$ (Park et al., 2019). Moreover, regional transport represents a significant influencing factor, with studies indicating substantial contributions to $PM_{10}$ concentrations from dust transport from northwestern regions and pollutant transport from surrounding urban agglomerations in spring (Ham et al., 2017).

The results indicate significant seasonal variations in monthly mean concentrations of organic matter (OM=1.4×OC) and elemental carbon (EC) in urban, rural, and urban-rural transition sites. All three functional site types showed the lowest concentrations in summer and the highest in winter, consistent with previous studies confirming the widespread winter-high and summer-low seasonal pattern of carbonaceous components in Chinese atmospheric particulates (Cao et al., 2007; Wang et al., 2016; Zhang et al., 2015). The elevated concentrations of OM and EC in winter correlate primarily with increased fossil fuel and biomass combustion emissions during the heating season, coupled with unfavorable meteorological dispersion conditions. Conversely, the decrease concentrations in summer are attributed to increased precipitation, increased mixing layer height, and reduced stationary source emissions due to higher temperatures. However, background sites showed different seasonal patterns than urban and peripheral sites, with OM and EC concentration peaks occurring in spring and fall. This phenomenon may be associated with regional-scale dust transport, biomass burning activities, and increased open-source emissions, while also reflecting minimal local anthropogenic influence at background sites, better representing regional background concentration variations.

We observed generally higher concentrations of $SO_4^{2-}$ and $NO_3^-$ in winter compared to lower concentrations in summer. This seasonal pattern is primarily due to increased $SO_2$ and $NO_x$ emissions from extensive fossil fuel combustion, especially coal, during the winter heating season, which provides abundant precursors for the formation of sulfate and nitrate. In addition, stable atmospheric stratification and frequent temperature inversions in winter inhibit the dispersion of pollutants, leading to near-surface accumulation of these secondary inorganic ions. Furthermore, the relatively lower temperatures in winter facilitate the gas-to-particle conversion of gaseous precursors, promoting the partitioning of semi-volatiles such as ammonium sulfate and ammonium nitrate to the particulate phase. In contrast, higher summer temperatures favor the gaseous state of these semi-volatile substances, while frequent convection and stronger atmospheric dispersion conditions significantly reduce sulfate and nitrate concentrations in $PM_{10}$ (Simonich and Hites, 1994). This seasonal pattern is consistent with observations from other regional studies and reflects the close relationship between secondary inorganic ion formation mechanisms and meteorological conditions (Liu et al., 2017a; Wang et al., 2023).

### 3.3 Oxidative potential (OP)

As shown in **Figure 8**, oxidative potential (OP) measurements conducted at twelve different sampling sites across China from June 2022 to May 2023 revealed significant temporal and spatial variability in $OP_v$. Further analysis revealed a strong correlation between $OP_v$ and the degree of urbanization at the sampling sites. During the sampling period, the urban site in Chengdu had significantly higher $OP_v$ levels compared to the other sites, while the rural site in Changde had the lowest $OP_v$ levels. However, the study revealed unexpectedly high average $OP_v$ levels at the rural site in Gucheng, ranking second highest

https://doi.org/10.5194/egusphere-2025-626
Preprint. Discussion started: 20 May 2025
© Author(s) 2025. CC BY 4.0 License.

among all sites, which may be closely related to its geographical location. Gucheng located in the Beijing-Tianjin-Hebei region, which is characterized by high population density and typical pollution concentration, the elevated $OP_v$ levels are likely due to the combined influence of pollutant transport from surrounding urban areas and local emissions (Han et al., 2015). In contrast, the urban site in Dalian demonstrated relatively low average $OP_v$ levels, ranking second lowest. This phenomenon may be attributed to the coastal location of Dalian, which benefits from strong marine air mass modulation and favorable atmospheric dispersion conditions(Meng et al., 2019), resulting in comparatively lower $OP_v$ levels.

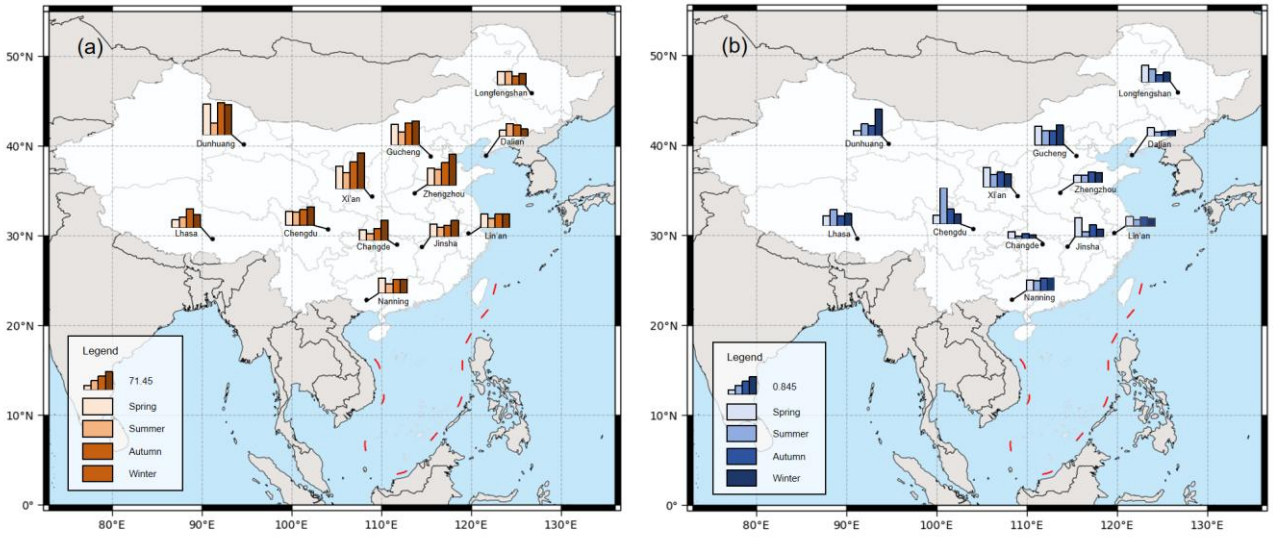


**Figure 8. Seasonal variations of (a) $PM_{10}$ concentrations（μg·m$^{-3}$） and (b) $OP_v$ (nmol $H_2O_2$·m$^{-3}$) across different regions of China. The map bases are from the Ministry of Natural Resources' Standard Map Service, review number GS(2019)1822.**

As shown in **Figure 8(a) and (b)**, sites located in northern Chinese sites exhibited significantly elevated $PM_{10}$ concentrations and $OP_v$ levels during the autumn and winter seasons. This phenomenon can be attributed to several concurrent factors. Firstly, the significant increase in coal and biomass combustion emissions (Liu et al., 2017b; Li et al., 2017) directly contributed to increased PM concentrations. Secondly, unfavorable meteorological conditions (Li et al., 2017), including low wind speeds, temperature inversions, and reduced atmospheric boundary layer height, significantly inhibited the ability of pollutants to disperse. Despite lower levels of urbanization in rural areas, $PM_{10}$ concentrations were comparable to urban areas due to the widespread use of solid fuels (Li et al., 2014). **Figure 8 (b)** shows that nine of the twelve sites had lower $OP_v$ values in summer. This may be due to more frequent rainfall, which reduces $PM_{10}$ concentrations and subsequently leads to lower $OP_v$ levels. However, sites such as Lhasa and Chengdu maintained relatively high $OP_v$ levels during the summer. This phenomenon may be related to the enhanced of photochemical reactions during summer, especially under conditions of high temperature and strong solar radiation, resulting in a significant increase in secondary organic aerosol (SOA) formation (Zhou et al., 2019; Saffari et al., 2014). In particular, Lhasa's high-altitude location, characterized by minimal precipitation and intense solar radiation, further promoted photochemical reactions, resulting in elevated $OP_v$ levels.

https://doi.org/10.5194/egusphere-2025-626
Preprint. Discussion started: 20 May 2025
© Author(s) 2025. CC BY 4.0 License.

We observed elevated $OP_v$ levels at background stations (such as Longfengshan, Jinsha, and Lin'an stations) in spring. This phenomenon may be attributed to the minimal influence of anthropogenic pollution sources at background stations, which typically exhibit more homogeneous mixing states and consequently have relatively lower and more stable $OP_v$ levels during other seasons. However, the frequent occurrence of dust storms and increased temperature inversion events during spring can lead to elevated particulate matter concentrations. In addition, the potential metal components carried by dust particles and the formation of secondary aerosols further enhance $OP_v$ levels(Saffari et al., 2014), resulting in significantly elevated $OP_v$ levels during spring.

**Table 4. Annual averaged $OP_v$ (nmol $H_2O_2$ $m^{-3}$) for $PM_{10}$ across different regions of China from June 2022 to May 2023.**

| Station | $OP_v$ | |
|---|---|---|
| | Average | Median |
| Chengdu | 0.85 | 0.57 |
| Dalian | 0.30 | 0.14 |
| Lhasa | 0.60 | 0.57 |
| Nanning | 0.56 | 0.50 |
| Xi'an | 0.73 | 0.74 |
| Changde | 0.22 | 0.21 |
| Gucheng | 0.83 | 0.75 |
| Dunhuang | 0.76 | 0.50 |
| Zhengzhou | 0.42 | 0.40 |
| Jinsha | 0.54 | 0.40 |
| Lin'an | 0.46 | 0.45 |
| Longfengshan | 0.57 | 0.52 |

As shown in **Figure 9(a)**, $OP_v$ concentrations in northern regions exhibited higher levels during the winter, primarily due to increased pollutant emissions associated with coal-based heating activities. In contrast, southern regions exhibited peak $OP_v$ concentrations in June, possibly due to enhanced photochemical reactions facilitated by stronger solar radiation intensity. However, a significant decrease was observed in July and August, which may be attributed to the increased frequency of precipitation events leading to enhanced wet deposition and removal particulate matter. **Figure 9 (b)** shows that the annual mean $OP_v$ concentrations in northern regions were significantly higher than those in southern regions ($p < 0.05$). This spatial variation can be attributed to several factors, including lower precipitation rates, frequent dust weather events, and emissions of coal combustion charactered in northern regions.

https://doi.org/10.5194/egusphere-2025-626
Preprint. Discussion started: 20 May 2025
© Author(s) 2025. CC BY 4.0 License.

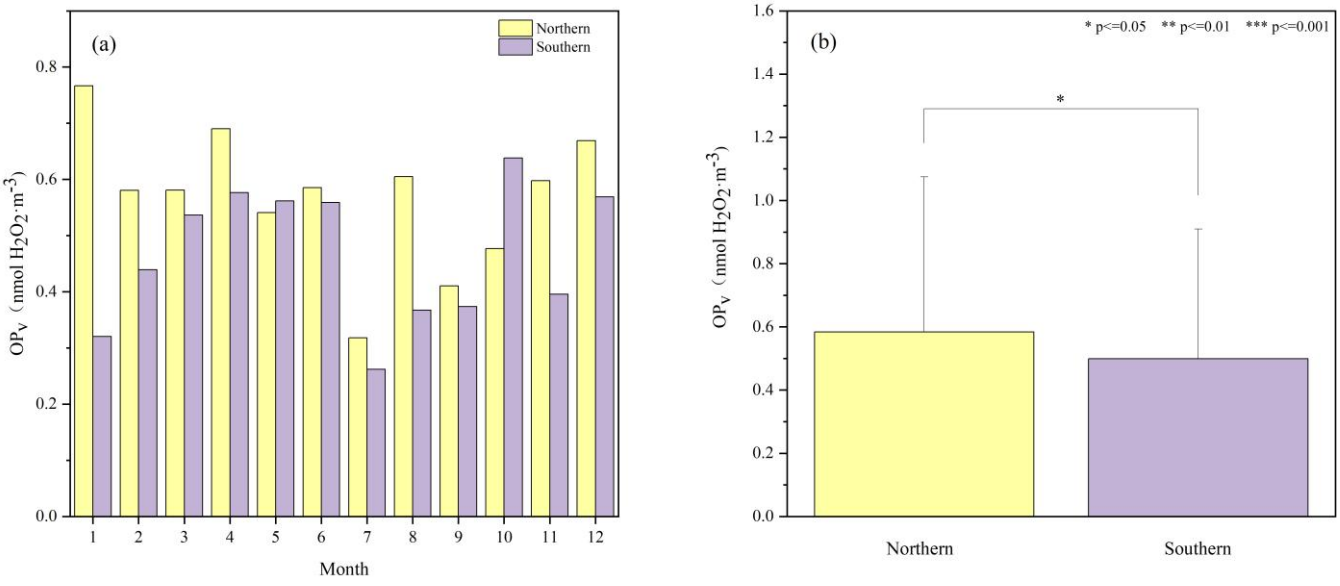


**Figure 9. Comparison of (a) monthly and (b) annual average $OP_v$ between sites in northern and southern China.**

### 3.4 Source appointment

#### 3.4.1 Source appointment of $PM_{10}$

This study employed the PMF model to conduct a detailed analysis of $PM_{10}$ sources at sites representing different regional types. The selected representative sites include the urban site Nanning (NN), background site Longfengshan (LFS), urban-rural junction site Zhengzhou (ZZ), and rural site Gucheng (GC). Results indicate that $PM_{10}$ in NN likely originates primarily from biomass burning, traffic, dust, secondary aerosols, and sea salt emissions. Sources of $PM_{10}$ in LFS may include biomass burning, traffic, dust, agricultural activities, and secondary aerosols. The $PM_{10}$ sources in ZZ are more complex, possibly including coal combustion emissions in addition to the aforementioned sources. $PM_{10}$ sources in GC are similar to those in ZZ, likely encompassing biomass burning, traffic, dust, agricultural activity emissions, secondary aerosols, and coal combustion emissions. **Figure 11** summarizes the distribution of $PM_{10}$ mass concentrations among the major sources at the four sites.

https://doi.org/10.5194/egusphere-2025-626
Preprint. Discussion started: 20 May 2025
© Author(s) 2025. CC BY 4.0 License.

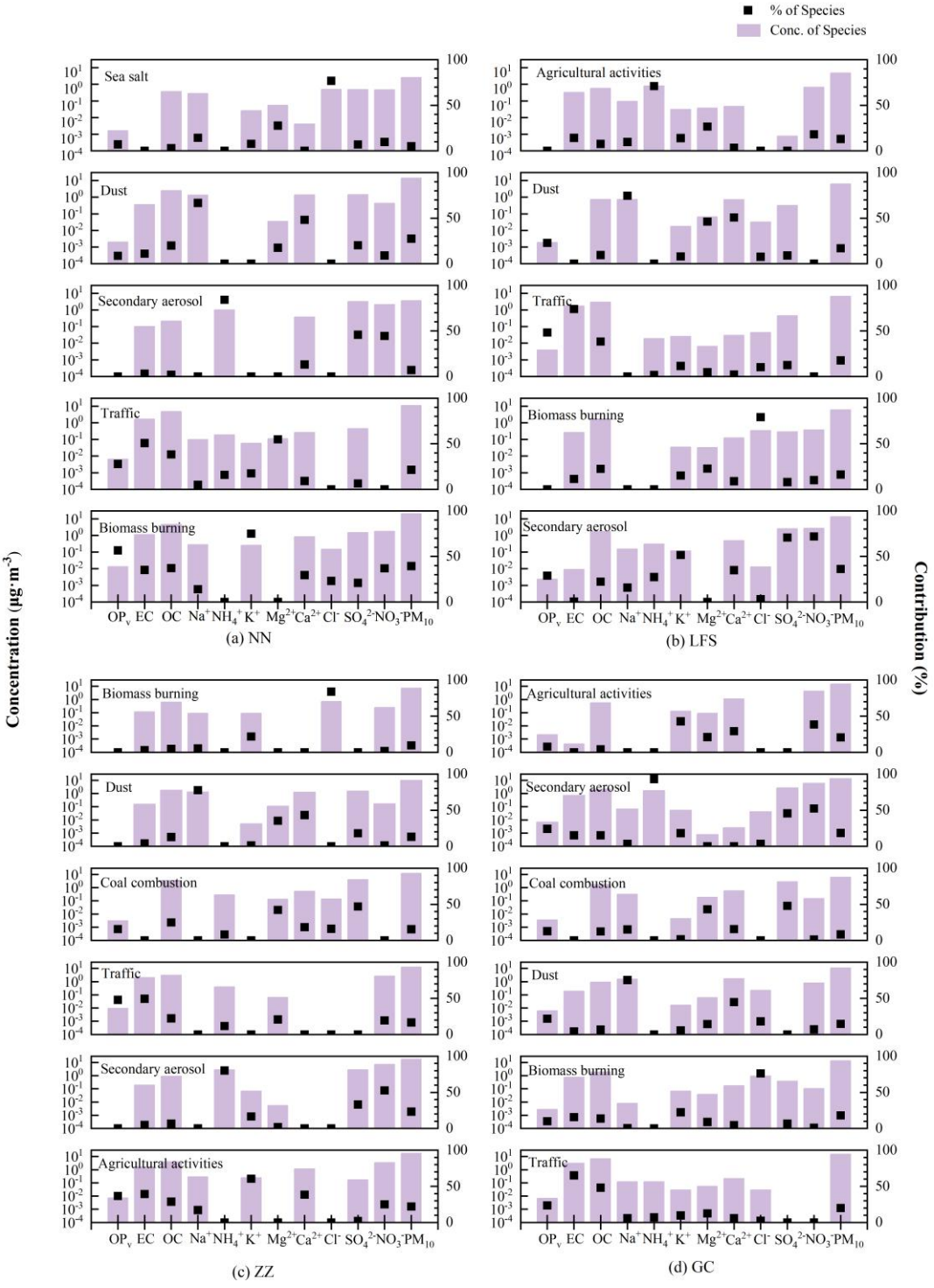


**Figure 10. Chemical profiles of the source factors identified at NN, LFS, ZZ and GC. The bars represent the chemical composition profiles (left y-axis) and the dots the explained variation values (right y-axis).**

https://doi.org/10.5194/egusphere-2025-626
Preprint. Discussion started: 20 May 2025
© Author(s) 2025. CC BY 4.0 License.

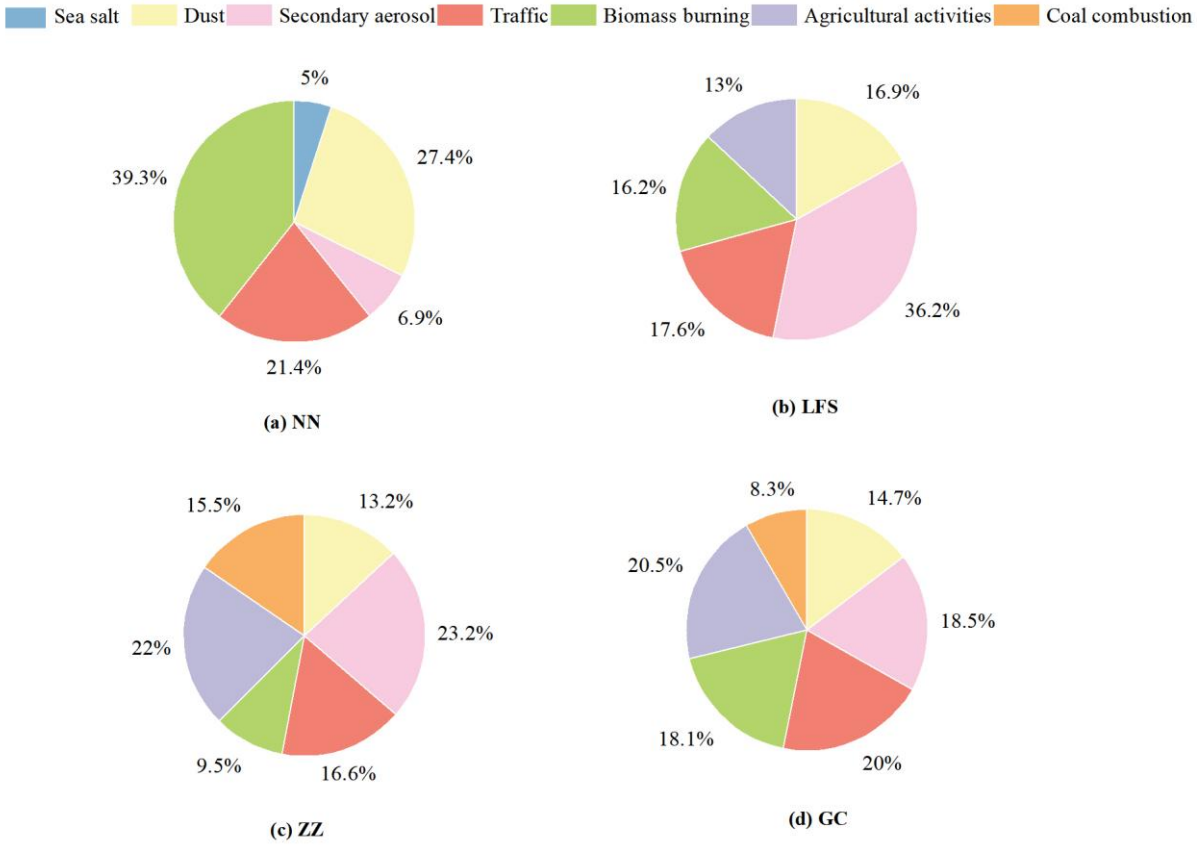


**Figure 11. The contributions of Biomass burning, Traffic, Dust, Secondary aerosol, Sea salt, Agricultural activities, and coal combustion to the atmospheric concentration of $PM_{10}$ mass (%) as derived by PMF modelling at NN, LFS, ZZ, and GC.**

As a typical urban site, the $PM_{10}$ source apportionment results at the NN site indicate that biomass burning, dust, and traffic are likely the main contributors, accounting for 39.3%, 27.4%, and 21.4% of total sources, respectively. As shown in **Figure 10**, the first factor contained high levels of $Cl^-$ (76.9%), $Mg^{2+}$ (27.6%), and $Na^+$ (14.3%), elements typically associated with sea salt (Viana et al., 2008), contributing approximately 5% to $PM_{10}$. Sea salt as a source of $PM_{10}$ in Nanning likely enters urban areas primarily through coastal air mass transport. Nanning is about 110 kilometers from the Beibu Gulf, and when prevailing southerly winds occur, sea salt aerosols from the South China Sea may migrate to inland cities through atmospheric circulation. The second factor contained high levels of $Na^+$ (66.7%), $Ca^{2+}$(48.1%) and $Mg^{2+}$ (17.5%), contributing approximately 26% to $PM_{10}$. This likely represents dust sources (Sharma et al., 2016), indicating that human activities such as urban construction may have some impact on particulate emissions. The third factor had high levels of $NH_4^+$ (84.2%), $SO_4^{2-}$ (45.7%), and $NO_3^-$ (44.4%), contributing approximately 6.9% to $PM_{10}$, possibly representing secondary aerosols. This suggests that the process of gaseous precursors (such as $SO_2$, $NO_x$, and VOCs) in the atmosphere forming secondary particles through photochemical reactions may have a certain impact on $PM_{10}$ concentrations(Yue et al., 2015). The fourth factor contained high

https://doi.org/10.5194/egusphere-2025-626
Preprint. Discussion started: 20 May 2025
© Author(s) 2025. CC BY 4.0 License.

levels of $Mg^{2+}$ (54.8%), EC (50.7%) and OC (38.2%), contributing approximately 20.2% to $PM_{10}$, possibly related to traffic. EC and OC have long been considered the main tracer elements for traffic emission sources, particularly vehicle exhaust emissions (Saarikoski et al., 2008; Sowlat et al., 2016; Esmaeilirad et al., 2020). Research has shown that Mg is one of the elements present in high concentrations in brake pad materials. Mg is typically used as a filler material in brake pads, and along with Fe, Ba and Cu, serves as a characteristic element of brake wear (Mckenzie et al., 2009). At the NN urban site, which is heavily influenced by traffic, brake wear is likely the primary source of these elements. The fifth factor had high levels of $K^+$ (74.9%), OC (37.2%), and EC (35.1%), substances typically associated with biomass burning (Stracquadanio et al., 2019). This factor made a significant contribution to urban $PM_{10}$ in Nanning, approximately 39.3%, indicating that biomass burning may be one of the important sources of atmospheric particulate pollution in Nanning. Although the observation point is located in the urban area of Nanning, which may be at some distance from areas where straw burning occurs, studies have shown that particulate matter produced by biomass burning may undergo long-distance transport (Uranishi et al., 2019).

The $PM_{10}$ source apportionment results for LFS indicate that secondary aerosols may be the main contributor, accounting for 36.2% of total sources. Source analysis identified five potential major factors: In the first factor, $NH_4^+$ (71.0%), $Mg^{2+}$ (26.5%), and $NO_3^-$ (18.0%) were present in high concentrations. $NH_4^+$ and $NO_3^-$ are the main nitrogen components in agricultural fertilizers (Hawkesford and Griffiths, 2019), while $Mg^{2+}$ is commonly added to fertilizers as a supplementary element (Lu et al., 2022). This factor may be related to agricultural activities, particularly fertilizer application processes. The second factor contained high levels of $Na^+$ (74.6%), $Mg^{2+}$ (46.2%), and $Ca^{2+}$ (50.8%), elements typically associated with dust sources(Zhang et al., 2014a; Sharma et al., 2016), contributing approximately 16.9% to $PM_{10}$. The third factor had high levels of EC (74.0%) and OC (38.3%), components typically associated with traffic (Esmaeilirad et al., 2020), contributing approximately 17.6%. The fourth factor contained high levels of $Cl^-$ (79.2%), $Mg^{2+}$ (22.7%), OC (22.5%), and $K^+$ (15.2%), among them, $K^+$ and $Cl^-$ have been identified as reliable indicators of biomass burning (Saggu and Mittal, 2020), contributing approximately 13% to $PM_{10}$. The fifth factor had high levels of $SO_4^{2-}$ (70.7%) and $NO_3^-$ (71.9%), with $NH_4^+$ (27.3%) also making a considerable contribution, these components are typically associated with secondary aerosol formation processes (Yue et al., 2015).

ZZ is located in a suburban area, and the diversity of its $PM_{10}$ sources may reflect the complex environmental characteristics of this region. Source apportionment results suggest that there may be six major pollution sources in this area, with their respective contribution proportions as follows: The first factor had high levels of $K^+$ (21.7%) and $Cl^-$ (83.9%), possibly indicating the influence of biomass burning (Saggu and Mittal, 2020), with a contribution proportion of approximately 9.5%. The second factor contained high levels of $Na^+$ (77.6%), $Mg^{2+}$ (35.3%), and $Ca^{2+}$ (43.2%), elements typically associated with dust sources(Sharma et al., 2016), contributing approximately 13.2% to $PM_{10}$. In the third factor, $Mg^{2+}$ (42.1%) and $SO_4^{2-}$-(46.9%) had relatively high concentrations. Since $SO_4^{2-}$ primarily originates from fuel combustion (Schwartz, 1993), combined with regional characteristics, this factor is associated with coal combustion emissions, contributing approximately 15.5% to $PM_{10}$. This coal combustion emission may be somewhat associated with combined heat and power facilities in the surrounding area. The fourth factor had high levels of EC (49.2%) and OC (22.1%), components typically associated with traffic (Esmaeilirad et al., 2020), contributing approximately 16.6%. The fifth factor contained high levels of $NH_4^+$ (80.1%), $SO_4^{2-}$

https://doi.org/10.5194/egusphere-2025-626
Preprint. Discussion started: 20 May 2025
© Author(s) 2025. CC BY 4.0 License.

(33.0%), and $NO_3^-$ (52.6%), components typically associated with secondary aerosol formation processes (Yue et al., 2015), accounting for approximately 23.2% of total $PM_{10}$ sources. The sixth factor had high levels of $K^+$ (60.6%), $Ca^{2+}$ (38.4%), EC (39.3%), and OC (28.8%); based on comprehensive analysis of these characteristic species, this factor may be related to agricultural activity emissions (Liu et al., 2023), contributing approximately 22% to $PM_{10}$.

The $PM_{10}$ source apportionment results for the GC show that agricultural activities, traffic emissions, secondary aerosols, and biomass burning are the main contributors, accounting for 20.5%, 20%, 18.5%, and 18.1% of total sources, respectively. The factor with $K^+$ (42.7%), $NO_3^-$ (38.4%), and $Ca^{2+}$ (29.2%) as primary characteristic species may be related to agricultural activities, accounting for 20.5%. This likely reflects the contribution of corn, wheat, and other farming activities around the site to $PM_{10}$, potentially associated with the agricultural-dominant economic structure of this rural area. The factor characterized by EC (65.1%) and OC (48.1%) likely comes from traffic (Esmaeilirad et al., 2020), representing the second-largest contributor to $PM_{10}$ at 20%. This indicates that transportation activities in rural areas may have a significant impact on $PM_{10}$ concentrations. The GC is relatively close to National Highway 107, and vehicle emissions from the highway may contribute to the site's $PM_{10}$ concentration through transport. Additionally, the increasing vehicle ownership in rural areas may be a contributing factor. Secondary aerosols, characterized by $NH_4^+$ (93.0%), $SO_4^{2-}$ (45.6%), and $NO_3^-$ (52.3%), account for 18.5%, indicating the important role of atmospheric secondary transformation processes in $PM_{10}$ formation in this region(Yue et al., 2015). The factor characterized by $K^+$ (22.3%) and $Cl^-$ (76.2%) may be related to biomass burning (Saggu and Mittal, 2020), accounting for 18.1%. This could be associated with activities such as straw burning and residential fuel use, particularly during crop harvest seasons and winter heating periods when such activities may increase. The factor characterized by $Na^+$ (75.2%) and $Ca^{2+}$ (44.6%) may be related to dust(Sharma et al., 2016), accounting for 14.7%, potentially reflecting the impact of agricultural cultivation and road dust on $PM_{10}$. The factor characterized by $Mg^{2+}$ (43.0%) and $SO_4^{2-}$ (47.8%) may be related to coal combustion emissions, accounting for 8.3%. This suggests that industrial activities and residential coal use in rural areas may have some impact on $PM_{10}$, especially during the winter heating season when such emissions may become more prominent.

### 3.4.2 Source appointment of OP in $PM_{10}$

This study utilized the PMF model to analyze the sources of $OP_v$ in $PM_{10}$ at four sites. As shown in **Figure 12**, vehicle emissions are a common significant contributor to $OP_v$ across the four sites: NN, LFS, ZZ, and GC, with contribution values of 28%, 48%, 48%, and 24%, respectively. The high contribution from vehicle emissions is mainly attributed to oxidative components in their particulate emissions, including organic carbon, polycyclic aromatic hydrocarbons, and transition metals. These components can directly or indirectly induce ROS generation, thereby enhancing the oxidative capacity of particulate matter (Valavanidis et al., 2008).

https://doi.org/10.5194/egusphere-2025-626
Preprint. Discussion started: 20 May 2025
© Author(s) 2025. CC BY 4.0 License.

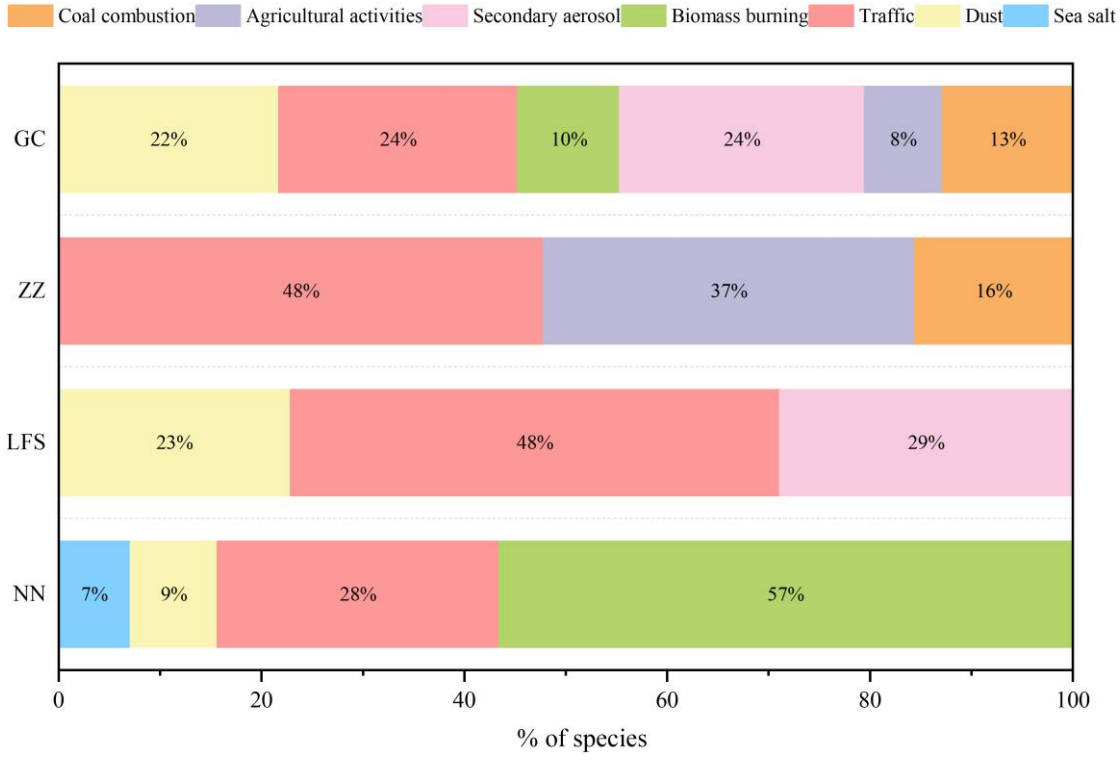


**Figure 12. The contributions of Biomass burning, Traffic, Dust, Secondary aerosol, Sea salt, Agricultural activities, and coal combustion to the atmospheric concentration of $OP_v$ (%) as derived by PMF modelling at NN, LFS, ZZ, and GC.**

The $OP_v$ at the NN mainly originates from biomass burning (57%) and traffic (28%), which is closely related to frequent crop straw burning activities and urban traffic emissions in the area. Additionally, 9% of the $OP_v$ at the NN site comes from dust and 7% from sea salt sources. The dust contribution in the Nanning area may be associated with local construction activities and road dust, as minerals and transition metal elements contained in dust can participate in ROS generation processes (Nishita-Hara et al., 2019; Lodovici and Bigagli, 2011). In addition, although Nanning is located inland, it is influenced by airflow from the South China Sea, which causes sea salt aerosols to affect the local atmospheric oxidative potential through long-range transport. Halogen compounds in sea salt (such as $Cl^-$, $Br^-$) can promote the generation of free radicals like OH· and Cl· through catalytic reactions, further participating in atmospheric oxidation processes(Cao et al., 2024; Knipping et al., 2000).

The $OP_v$ contribution at the LFS mainly comes from traffic (48%), agricultural activities (29%), and dust (23%). As a site in the Wuchang area of Heilongjiang province, LFS is surrounded by extensive farmland. Particulate matter emitted from agricultural activities contains secondary inorganic components such as nitrates and ammonium salts, which can participate in ROS generation processes through various pathways (Lodovici and Bigagli, 2011). Additionally, the dry climate conditions in the north lead to significant dust contributions. Transition metals contained in dust can catalyze ROS generation, enhancing the oxidative capacity of particulate matter (Saffari et al., 2014).

https://doi.org/10.5194/egusphere-2025-626
Preprint. Discussion started: 20 May 2025
© Author(s) 2025. CC BY 4.0 License.

The $OP_v$ at the ZZ mainly originates from traffic (48%), agricultural activities (37%), and coal combustion (16%). As an important transportation hub city in the central region, Zhengzhou has a large number of vehicles, and exhaust emissions significantly impact atmospheric oxidative capacity. Meanwhile, the extensive distribution of farmland around Zhengzhou makes agricultural source emissions an important factor affecting urban atmospheric oxidative capacity. Furthermore, coal combustion contributes 16% to the $OP_v$ at the ZZ site, possibly related to the continuing coal consumption in the area. Particulate matter emitted during coal combustion processes contains numerous transition metals (such as Fe, Cu, Mn, etc.) and polycyclic aromatic hydrocarbons, which can promote ROS generation through pathways such as Fenton reactions, enhancing the oxidative potential of particulate matter (Pardo et al., 2020).

The $OP_v$ source composition at the GC is the most complex, exhibiting diverse pollution characteristics. Through detailed analysis, the $OP_v$ sources at this site primarily include six categories: traffic account for 24%, secondary aerosols 24%, dust 22%, coal combustion 13%, biomass burning 10%, and agricultural activities 8%. This complex source composition reflects the diversity and comprehensive nature of regional pollution. Compared to other sites, the contribution proportion of coal combustion sources at the GC site is relatively low, which may be due to the energy structure transition or differences in usage intensity in this region. Notably, the contribution of secondary aerosols at the GC site is significantly higher than at other monitoring points, accounting for nearly a quarter of the total sources. This characteristic indicates that in the atmospheric particulate formation process of this region, secondary transformation processes play a crucial role, significantly affecting atmospheric oxidation capacity and particulate generation mechanisms.

## 4 Conclusions

This study utilized a comprehensive approach to analyze the characteristics and sources of $PM_{10}$ and its oxidative potential (OP) at 12 representative sites in China. The main findings are summarized as follows:

1. Performance of CNN-LSTM deep learning model

The CNN-LSTM deep learning model exhibited robust performance in reconstructing missing data for $PM_{10}$ mass concentrations and outliers in chemical components. The model achieved $R^2$ values of 0.967 and 0.884 for the training and testing sets, respectively. These results highlight the potential of the model to address missing data issues in $PM_{10}$ research.

2. Spatiotemporal variations in $PM_{10}$ and OP levels

$PM_{10}$ and OP concentrations showed remarkable spatial and temporal variations:

- $PM_{10}$ concentrations were relatively higher in Xi'an and Dunhuang in the northwestern region, while lower in Longfengshan and Dalian in the northeastern region.
- Suburban sites generally exhibited higher $PM_{10}$ concentrations compared to other site types.
- OP levels were relatively higher in Chengdu and Gucheng, with urban sites having higher $OP_v$ values than other sites.
- Annual average $PM_{10}$ concentrations in northern regions were typically higher than in southern regions.

https://doi.org/10.5194/egusphere-2025-626
Preprint. Discussion started: 20 May 2025
© Author(s) 2025. CC BY 4.0 License.

- Seasonally, $PM_{10}$ and OP levels were higher in winter and lower in summer, suggesting the potential benefits of implementing targeted control measures during high-risk periods to mitigate adverse health impacts.

3. Source Apportionment Findings

Source apportionment using PMF indicated that dust, biomass burning, traffic emissions, and agricultural activities were likely the main contributing sources to $PM_{10}$ mass concentrations at the study sites. Understanding the contributions of these sources is crucial for developing more effective $PM_{10}$ reduction strategies.

4. Oxidative Potential Source Analysis

The $OP_v$ source apportionment conducted using PMF indicates that vehicle emissions may be one of the important sources of OP at the four sites—NN, LFS, ZZ, and GC—accounting for 24-48%. There are significant differences in source profiles among the sites: NN is dominated by biomass burning (57%) and traffic (28%); LFS is mainly characterized by traffic (48%), Secondary aerosol (29%), and dust (23%); ZZ is primarily influenced by traffic (48%) and agricultural activities (37%); GC has the most complex source profile, with comparable contributions from multiple sources including traffic, secondary aerosols, and dust. The differences between sites suggest that the sources of atmospheric particulate oxidative potential have distinct regional characteristics. It is recommended to adopt targeted differentiated control strategies, especially strengthening the regulation of vehicle emissions.

The study results underscore the importance of identifying and quantifying OP sources to assess and mitigate health risks associated with $PM_{10}$ exposure. The source apportionment findings suggest that emission reduction measures targeting traffic, biomass burning, dust, and agricultural activities may help lower OP levels and protect public health. This research employed deep learning techniques to analyze the spatiotemporal distribution characteristics, source apportionment, and influencing factors of $PM_{10}$ and its OP in different typical regions of China from multiple perspectives. The findings provide a scientific basis for better understanding the causes of $PM_{10}$ pollution, formulating control strategies, and mitigating health risks. Future studies should focus on further investigating the identification and health risk assessment of toxic and harmful components in $PM_{10}$, exploring the toxicological mechanisms of OP, and developing integrated indicators that combine chemical components and toxicity for characterizing and evaluating $PM_{10}$ pollution.

**Code availability.** The software code is available upon request.

**Data availability.** The data used in this study are available on the Zenodo data repository platform at https://doi.org/10.5281/zenodo.15420768.

**Author contribution.** Q.C.: Software, Writing – original draft preparation. D.F. and J.J.: Data curation, Conceptualization, Writing – review & editing. X. H.: Management of OP measurements. Y.C.: Methodology, Investigation. T.Z. and Y.B.: Software, Methodology. Y. Z.: Conceptualization, Writing – review & editing.

**Competing interests.** The authors declare that they have no conflict of interest.

**Disclaimer.** Publisher's note: Copernicus Publications remains neutral with regard to jurisdictional claims in published maps and institutional affiliations.

https://doi.org/10.5194/egusphere-2025-626
Preprint. Discussion started: 20 May 2025
© Author(s) 2025. CC BY 4.0 License.

**Financial support.** This work was supported by the National Natural Science Foundation of China (No. 21677145), the Fundamental Research Funds for the Central Universities (No. E0E48927X2) and the Foundation of CMA Meteorological Observation Center (#MOCQN202409).

**Acknowledgments:** The authors are grateful to the study participants and field staff in the twelve stations of the CMA Atmosphere Watch Network (CAWNET).

https://doi.org/10.5194/egusphere-2025-626
Preprint. Discussion started: 20 May 2025
© Author(s) 2025. CC BY 4.0 License.

## References

An, J. Q., Liu, H. B., Wang, X. M., Talifu, D., Abulizi, A., Maihemuti, M., Li, K. J., Bai, H. F., Luo, P., and Xie, X. X.: Oxidative potential of size-segregated particulate matter in the dust-storm impacted Hotan, northwest China, Atmos. Environ., 280, https://doi.org/10.1016/j.atmosenv.2022.119142, 2022.

Antonini, J. M., Clarke, R. W., Murthy, G. G. K., Sreekanthan, P., Jenkins, N., Eagar, T. W., and Brain, J. D.: Freshly generated stainless steel welding fume induces greater lung inflammation in rats as compared to aged fume, Toxicol. Lett., 98, 77-86, https://doi.org/10.1016/s0378-4274(98)00103-9, 1998.

Bates, J. T., Fang, T., Verma, V., Zeng, L. H., Weber, R. J., Tolbert, P. E., Abrams, J. Y., Sarnat, S. E., Klein, M., Mulholland, J. A., and Russell, A. G.: Review of Acellular Assays of Ambient Particulate Matter Oxidative Potential: Methods and Relationships with Composition, Sources, and Health Effects, Environ. Sci. Technol., 53, 4003-4019, https://doi.org/10.1021/acs.est.8b03430, 2019.

Borlaza, L. J., Weber, S., Marsal, A., Uzu, G., Jacob, V., Besombes, J. L., Chatain, M., Conil, S., and Jaffrezo, J. L.: Nine-year trends of $PM_{10}$ sources and oxidative potential in a rural background site in France, Atmos. Chem. Phys., 22, 8701-8723, https://doi.org/10.5194/acp-22-8701-2022, 2022.

Cao, J. J., Lee, S. C., Chow, J. C., Watson, J. G., Ho, K. F., Zhang, R. J., Jin, Z. D., Shen, Z. X., Chen, G. C., Kang, Y. M., Zou, S. C., Zhang, L. Z., Qi, S. H., Dai, M. H., Cheng, Y., and Hu, K.: Spatial and seasonal distributions of carbonaceous aerosols over China, Journal of Geophysical Research-Atmospheres, 112, https://doi.org/10.1029/2006jd008205, 2007.

Cao, L. M., Zhou, Y., Zhang, Z., Sun, W. W., and Chen, W. H.: Impacts of airborne particulate matter and its components on respiratory system health, Chinese journal of preventive medicine, 50, 1114-1118, http://dx.doi.org/10.3760/cma.j.issn.0253-9624.2016.12.018, 2016.

Cao, Y. Q., Wang, Z., Liu, J. R., Ma, Q. X., Li, S. Y., Liu, J., Li, H., Zhang, P., Chen, T. Z., Wang, Y. H., Chu, B. W., Zhang, X. H., Saiz-Lopez, A., Francisco, J. S., and He, H.: Spontaneous Molecular Bromine Production in Sea-Salt Aerosols, Angewandte Chemie-International Edition, 63, https://doi.org/10.1002/anie.202409779, 2024.

Chirino, Y. I., Sánchez-Pérez, Y., Osornio-Vargas, á. R., Morales-Bárcenas, R., Gutiérrez-Ruíz, M. C., Segura-García, Y., Rosas, I., Pedraza-Chaverri, J., and Garcia-Cuellar, C. M.: $PM_{10}$ impairs the antioxidant defense system and exacerbates oxidative stress driven cell death, Toxicol. Lett.,193, 209-216, http://dx.doi.org/10.1016/j.toxlet.2010.01.009, 2010.

Cohen, A. J., Ross Anderson, H., Ostro, B., Pandey, K. D., Krzyzanowski, M., Künzli, N., Gutschmidt, K., Pope, A., Romieu, I., Samet, J. M., Smith, K.: The global burden of disease due to outdoor air pollution, Journal of Toxicology and Environmental Health Part A Current Issues, 68, 1301-1307, http://dx.doi.org/10.1080/15287390590936166, 2005.

Cohn, C. A., Simon, S. R., and Schoonen, M. A. A.: Comparison of fluorescence-based techniques for the quantification of particle-induced hydroxyl radicals, Part. Fibre Toxicol., 5, http://dx.doi.org/10.1186/1743-8977-5-2, 2008.

Cui, R., Guo, X. B., Deng, F. R., Liu, H.: Analysis of Water-soluble Ions and Elements in $PM_{10}$ and $PM_{2.5}$, Journal of Environment and Health, 25, 291-294, http://dx.doi.org/10.3969/j.issn.1001-5914.2008.04.003, 2008.

https://doi.org/10.5194/egusphere-2025-626
Preprint. Discussion started: 20 May 2025
© Author(s) 2025. CC BY 4.0 License.

Domingos, J. S. S., Regis, A. C. D., Santos, J. V. S., de Andrade, J. B., and da Rocha, G. O.: A comprehensive and suitable method for determining major ions from atmospheric particulate matter matrices, J. Chromatogr. A, 1266, 17-23, http://dx.doi.org/10.1016/j.chroma.2012.08.074, 2012.

Esmaeilirad, S., Lai, A., Abbaszade, G., Schnelle-Kreis, J., Zimmermann, R., Uzu, G., Daellenbach, K., Canonaco, F., Hassankhany, H., Arhami, M., Baltensperger, U., Prévôt, A. S. H., Schauer, J. J., Jaffrezo, J. L., Hosseini, V., and El Haddad, I.: Source apportionment of fine particulate matter in a Middle Eastern Metropolis, Tehran-Iran, using PMF with organic and inorganic markers, Sci. Total Environ., 705, http://dx.doi.org/10.1016/j.scitotenv.2019.135330, 2020.

Gao, D., Ripley, S., Weichenthal, S., and Pollitt, K. J. G.: Ambient particulate matter oxidative potential: Chemical determinants, associated health effects, and strategies for risk management, Free Radical Biology and Medicine, 151, 7-25, http://dx.doi.org/10.1016/j.freeradbiomed.2020.04.028, 2020.

Ghio, A. J., Carraway, M. S., and Madden, M. C.: Composition of Air Pollution Particles and Oxidative Stress in Cells, Tissues, and Living Systems, Journal of Toxicology and Environmental Health-Part B-Critical Reviews, 15, 1-21, http://dx.doi.org/10.1080/10937404.2012.632359, 2012.

Guo, H. B., Jin, L., and Huang, S. J.: Effect of PM characterization on PM oxidative potential by acellular assays: a review, Rev. Environ. Health, 35, 461-470, http://dx.doi.org/10.1515/reveh-2020-0003, 2020.

Ham, J., Lee, H. J., Cha, J. W., and Ryoo, S. B.: Potential Source of $PM_{10}$, $PM_{2.5}$, and OC and EC in Seoul During Spring 2016, Atmosphere-Korea, 27, 41-54, http://dx.doi.org/10.14191/Atmos.2017.27.1.041, 2017.

Han, L. J., Zhou, W. Q., and Li, W. F.: Increasing impact of urban fine particles ($PM_{2.5}$) on areas surrounding Chinese cities, Scientific Reports, 5, http://dx.doi.org/10.1038/srep12467, 2015.

Hawkesford, M. J. , Griffiths, S .:Exploiting genetic variation in nitrogen use efficiency for cereal crop improvement[J].Current Opinion in Plant Biology, 49, 35-42. http://dx.doi.org/10.1016/j.pbi.2019.05.003, 2019.

He, L. C. and Zhang, J. F.: Particulate matter (PM) oxidative potential: Measurement methods and links to PM physicochemical characteristics and health effects, Crit. Rev. Environ. Sci. Technol., 53, 177-197, http://dx.doi.org/10.1080/10643389.2022.2050148, 2023.

Hedayat, F., Stevanovic, S., Milic, A., Miljevic, B., Nabi, M. N., Zare, A., Bottle, S. E., Brown, R. J., and Ristovski, Z. D.: Influence of oxygen content of the certain types of biodiesels on particulate oxidative potential, Sci. Total Environ., 545, 381-388, http://dx.doi.org/10.1016/j.scitotenv.2015.12.036, 2016.

Hochreiter, S. and Schmidhuber, J.: Long Short-term Memory, Neural Comput., 9, 1735-1780, https://doi.org/10.1162/neco.1997.9.8.1735, 1997.

Huang, C. J. and Kuo, P. H.: A Deep CNN-LSTM Model for Particulate Matter ($PM_{2.5}$) Forecasting in Smart Cities, Sensors, 18, https://doi.org/10.3390/s18072220, 2018.

Huang, W., Zhang, Y., Zhang, Y., Fang, D., and Schauer, J. J.: Optimization of the Measurement of Particle-Bound Reactive Oxygen Species with 2′,7′-dichlorofluorescin (DCFH), Water, Air, & Soil Pollution, 227, 164, https://doi.org/10.1007/s11270-016-2860-9, 2016.

https://doi.org/10.5194/egusphere-2025-626
Preprint. Discussion started: 20 May 2025
© Author(s) 2025. CC BY 4.0 License.

Huang, X. J. A.: The Impact of $PM_{10}$ and Other Airborne Particulate Matter on the Cardiopulmonary and Respiratory Systems of Sports Personnel under Atmospheric Exposure, Atmosphere, 14, https://doi.org/10.3390/atmos14111697, 2023.

Jiao, J., Jia, X. F., Yan, P., Cao, F., Fang, D.Q., Ma, Q.L., Yu, D.J., Chu, J. H.: Chemical characterization of $PM_{10}$ in the east-central background region of China, 2016-2017. Journal of Applied Meteorological Science, 32, 65-77, https://doi.org/10.11898/1001-7313.20210106, 2021.

Knipping, E. M., Lakin, M. J., Foster, K. L., Jungwirth, P., Tobias, D. J., Gerber, R. B., Dabdub, D., and Finlayson-Pitts, B. J.: Experiments and simulations of ion-enhanced interfacial chemistry on aqueous NaCl aerosols, Science, 288, 301-306, https://doi.org/10.1126/science.288.5464.301, 2000.

Lee, S. M., Shin, J.: Hybrid Model of Convolutional LSTM and CNN to Predict Particulate Matter, International Journal of Information and Electronics Engineering, https://doi.org/ 10.18178/IJIEE.2019.9.1.701, 2019.

Li, H., Zhang, Q., Zhang, Q., Chen, C., Wang, L., Wei, Z., Zhou, S., Parworth, C., Zheng, B., Canonaco, F. J.: Wintertime aerosol chemistry and haze evolution in an extremely polluted city of the North China Plain: significant contribution from coal and biomass combustion, Atmos. Chem. Phys. ,17, 1-31, http://dx.doi.org/10.5194/acp-17-4751-2017, 2017.

Li, N., Hao, M., Phalen, R. F., Hinds, W. C., and Nel, A. E.: Particulate air pollutants and asthma: A paradigm for the role of oxidative stress in PM-induced adverse health effects, Clin. Immunol., 109, 250, http://dx.doi.org/10.1016/j.clim.2003.08.006 2003.

Li, Q. F., Wyatt, A., and Kamens, R. M.: Oxidant generation and toxicity enhancement of aged-diesel exhaust, Atmos. Environ., 43, 1037-1042, http://dx.doi.org/10.1016/j.atmosenv.2008.11.018, 2009.

Li, T. Y., Hua, M., and Wu, X.: A Hybrid CNN-LSTM Model for Forecasting Particulate Matter ($PM_{2.5}$), Ieee Access, 8, 26933-26940, http://dx.doi.org/10.1109/access.2020.2971348, 2020.

Li, W., Wang, C., Wang, H. Q. J., Chen, J. W., Yuan, C. Y., Li, T. C., Wang, W. T., Shen, H. Z., Huang, Y., Wang, R., Wang, B., Zhang, Y. Y., Chen, H., Chen, Y. C., Tang, J. H., Wang, X. L., Liu, J. F., Coveney, R. M., and Tao, S.: Distribution of atmospheric particulate matter (PM) in rural field, rural village and urban areas of northern China, Environ. Pollut., 185, 134-140, http://dx.doi.org/10.1016/j.envpol.2013.10.042, 2014.

Li, X., Song, H., Zhai, S., Lu, S., Kong, Y., Xia, H., and Zhao, H.: Particulate matter pollution in Chinese cities: Areal-temporal variations and their relationships with meteorological conditions (2015-2017), Environ. Pollut., 246, http://dx.doi.org/10.1016/j.envpol.2018.11.103, 2019.

Liang, T., Xie, G., Mi, D., and Jiang, W.: Prediction of $PM_{10}$ Concentraion Based on CEEMDAN-SE and LSTM Neural Network, Environment Engineering, 38, 107-113, http://dx.doi.org/10.1109/EI247390.2019.9061986, 2020.

Liu, H. X., Zheng, J. R., Qu, C. K., Zhang, J. Q., Wang, Y. K., Zhan, C. L., Yao, R. Z., and Cao, J. J.: Characteristics and Source Analysis of Water-Soluble Inorganic Ions in $PM_{10}$ in a Typical Mining City, Central China, Atmosphere, 8, http://dx.doi.org/10.3390/atmos8040074, 2017a.

https://doi.org/10.5194/egusphere-2025-626
Preprint. Discussion started: 20 May 2025
© Author(s) 2025. CC BY 4.0 License.

Liu, P., Zhang, C., Mu, Y., Liu, C., Xue, C., Ye, C., Liu, J., Zhang, Y., Zhang, H.: The possible contribution of the periodic emissions from farmers' activities in the North China Plain to atmospheric water-soluble ions in Beijing, Atmos. Chem. Phys.,16, http://dx.doi.org/10.5194/acp-16-10097-2016, 2016.

Liu, P., Zhang, C., Xue, C., Mu, Y., Liu, J., Zhang, Y., Tian, D., Ye, C., Zhang, H., Guan, J.: The contribution of residential coal combustion to atmospheric $PM_{2.5}$ in northern China during winter, Atmos. Chem. Phys., 17, 1-37, http://dx.doi.org/10.5194/acp-17-11503-2017, 2017b.

Lodovici, M. and Bigagli, E.: Oxidative Stress and Air Pollution Exposure, Journal of Toxicology, 2011, http://dx.doi.org/10.1155/2011/487074, 2011.

Lu, Z., Wang, Y., Degryse, F., Huang, C., Hou, C.,Wu, L., Jiang, R., Mclaughlin, M. J., and Zhang, F. : Magnesium-fortified phosphate fertilizers improve nutrient uptake and plant growth without reducing phosphorus availability, Pedosphere, 32, 744-751, http://dx.doi.org/10.1016/j.pedsph.2022.06.010, 2022.

McKenzie, E. R., Money, J. E., Green, P. G., and Young, T. M.: Metals associated with stormwater-relevant brake and tire samples, Sci. Total Environ., 407, 5855-5860, http://dx.doi.org/10.1016/j.scitotenv.2009.07.018, 2009.

Meng, L., Li, Y., Han, S., and Hao, T.: Influence of Sea-Land Breeze on the Concentrations of $PM_{2.5}$ and $O_3$ in Tianjin City, Research of Environmental Sciences, 32, 390-398, http://dx.doi.org/ 10. 13198/j. issn. 1001-6929. 2018. 12. 10, 2019.

Nishita-Hara, C., Hirabayashi, M., Hara, K., Yamazaki, A., and Hayashi, M.: Dithiothreitol-Measured Oxidative Potential of Size-Segregated Particulate Matter in Fukuoka, Japan: Effects of Asian Dust Events, Geohealth, 3, 160-173, http://dx.doi.org/10.1029/2019gh000189, 2019.

Okut, H.: Deep Learning for Subtyping and Prediction of Diseases: Long-Short Term Memory, http://dx.doi.org/10.5772/intechopen.96180, 2021.

Paatero, P.: Least squares formulation of robust non-negative factor analysis, Chemom. Intell. Lab. Syst., 37, 23-35, http://dx.doi.org/10.1016/s0169-7439(96)00044-5, 1997.

Paatero, P. and Tapper, U. J. E.: Positive matrix factorization: A nonnegative factor model with optimal utilization of error estimates of data values, Environmetrics, 5, http://dx.doi.org/10.1002/env.3170050203, 1994.

Pardo, M., Qiu, X. H., Zimmermann, R., and Rudich, Y.: Particulate Matter Toxicity Is Nrf2 and Mitochondria Dependent: The Roles of Metals and Polycyclic Aromatic Hydrocarbons, Chem. Res. Toxicol., 33, 1110-1120, http://dx.doi.org/10.1021/acs.chemrestox.0c00007, 2020.

Park, I. S., Kim, H. K., Song, C. K., Jang, Y. W., Kim, S. H., Cho, C. R., Owen, J. S., Kim, C. H., Chung, K. W., and Park, M. S.: Meteorological Characteristics and Assessment of the Effect of Local Emissions during High $PM_{10}$ Concentration in the Seoul Metropolitan Area, Asian J. Atmos. Environ., 13, 117-135, http://dx.doi.org/10.5572/ajae.2019.13.2.117, 2019.

Qin, D. M., Yu, J., Zou, G. J., Yong, R. H., Zhao, Q., and Zhang, B.: A Novel Combined Prediction Scheme Based on CNN and LSTM for Urban $PM_{2.5}$ Concentration, Ieee Access, 7, 20050-20059, http://dx.doi.org/10.1109/access.2019.2897028, 2019.

https://doi.org/10.5194/egusphere-2025-626
Preprint. Discussion started: 20 May 2025
© Author(s) 2025. CC BY 4.0 License.

Qu, W. J., Arimoto, R., Zhang, X. Y., Zhao, C. H., Wang, Y. Q., Sheng, L. F., Fu, G.: Spatial distribution and interannual variation of surface $PM_{10}$ concentrations over eighty-six Chinese cities, Atmos. Chem. Phys., 10, 5641-5662, http://dx.doi.org/10.5194/acp-10-5641-2010, 2010.

Saarikoski, S. K., Sillanpää, M. K., Saarnio, K. M., Hillamo, R. E., Pennanen, A. S., and Salonen, R. O.: Impact of biomass combustion on urban fine particulate matter in Central and Northern Europe, Water Air and Soil Pollution, 191, 265-277, http://dx.doi.org/10.1007/s11270-008-9623-1, 2008.

Saffari, A., Daher, N., Shafer, M. M., Schauer, J. J., and Sioutas, C.: Global perspective on the oxidative potential of airborne particulate matter: A synthesis of research findings, Environ. Sci. Technol., 48, 7576, http://dx.doi.org/10.1021/es500937x, 2014.

Saggu, G. S. and Mittal, S. K.: Source apportionment of $PM_{10}$ by positive matrix factorization model at a source region of biomass burning, J. Environ. Manage., 266, http://dx.doi.org/10.1016/j.jenvman.2020.110545, 2020.

Schwartz, S. E. J. E.: Does fossil fuel combustion lead to global warming?, Energy, 18, 1229-1248, http://dx.doi.org/10.1016/0360-5442(93)90012-3, 1993.

Shao, L. Y., Shi, Z. B, and Qin, H.: A Study of Inhalable Particles in the Urban Ambient Air, Environmental protection , http://dx.doi.org/10.3969/j.issn.0253-9705.2000.01.010, 2000.

Sharma, S. K., Mandal, T. K., Jain, S., Saraswati, Sharma, A., and Saxena, M.: Source Apportionment of $PM_{2.5}$ in Delhi, India Using PMF Model, Bull. Environ. Contam. Toxicol., 97, 286-293, http://dx.doi.org/10.1007/s00128-016-1836-1, 2016.

Shen, Z. X., Sun, J., Cao, J.J., Zhang, L. M., Zhang, Q., Lei, Y. L., Gao, J. J., Huang, R. J., Liu, S. X, Huang, Y., Zhu, C. S., Xu, H. M., Zheng, C. L., Liu, P. P., Xue. Z. G.: Chemical profiles of urban fugitive dust $PM_{2.5}$ samples in Northern Chinese cities, Sci. Total Environ. 569-570, 619-626, http://dx.doi.org/10.1016/j.scitotenv.2016.06.156, 2016.

Sherstinsky, A.: Fundamentals of Recurrent Neural Network (RNN) and Long Short-Term Memory (LSTM) network, Physica D-Nonlinear Phenomena, 404, http://dx.doi.org/10.1016/j.physd.2019.132306, 2020.

Shi, J., Yan, J. P., Wang, S. S., Zhao, S. H., Zhang, M. M., Xu, S. Q., Lin, Q., and Yang, H.: Determinant of Sea Salt Aerosol Emission in the Southern Hemisphere in Summer Time, Earth and Space Science, 9, http://dx.doi.org/10.1029/2022ea002529, 2022.

Simonich, S. L. and Hites, R. A.: Vegetation-Atmosphere Partitioning of Polycyclic Aromatic Hydrocarbons, Environ. Sci. Technol., 28, 939-943, http://dx.doi.org/10.1021/es00054a028, 1994.

Sowlat, M. H., Hasheminassab, S., and Sioutas, C.: Source apportionment of ambient particle number concentrations in central Los Angeles using positive matrix factorization (PMF), Atmos. Chem. Phys., 16, 4849-4866, http://dx.doi.org/10.5194/acp-16-4849-2016, 2016.

Stracquadanio, M., Petralia, E., Berico, M., La Torretta, T. M. G., Malaguti, A., Mircea, M., Gualtieri, M., and Ciancarella, L.: Source Apportionment and Macro Tracer: Integration of Independent Methods for Quantification of Woody Biomass Burning Contribution to $PM_{10}$, Aerosol Air Qual. Res., 19, 711-723, http://dx.doi.org/10.4209/aaqr.2018.05.0186, 2019.

© Author(s) 2025. CC BY 4.0 License.

Tsvetanova, I., Zheleva, I., Filipova, M., and Stefanova, A.: Statistical analysis of ambient air $PM_{10}$ contamination during winter periods for Ruse region, Bulgaria, 13th National Congress on Theoretical and Applied Mechanics (NCTAM), Bulgarian Acad Sci, Inst Mech Campus I, Sofia, BULGARIA, Sep 06-10, http://dx.doi.org/10.1051/matecconf/201814501007, 2018.

Uranishi, K., Ikemori, F., Shimadera, H., Kondo, A., and Sugata, S.: Impact of field biomass burning on local pollution and long-range transport of $PM_{2.5}$ in Northeast Asia, Environ. Pollut., 244, 414-422, http://dx.doi.org/10.1016/j.envpol.2018.09.061, 2019.

Valavanidis, A., Fiotakis, K., and Vlachogianni, T.: Airborne Particulate Matter and Human Health: Toxicological Assessment and Importance of Size and Composition of Particles for Oxidative Damage and Carcinogenic Mechanisms, Journal of Environmental Science and Health Part C-Environmental Carcinogenesis & Ecotoxicology Reviews, 26, 339-362, http://dx.doi.org/10.1080/10590500802494538, 2008.

Vennerød, C. B., Kjærran, A., and Bugge, E. S. J. A.: Long Short-term Memory RNN, http://arxiv.org/abs/2105.06756, 2021.

Verma, V., Fang, T., Xu, L., Peltier, R. E., Russell, A. G., Ng, N. L., and Weber, R. J.: Organic Aerosols Associated with the Generation of Reactive Oxygen Species (ROS) by Water-Soluble $PM_{2.5}$, Environ. Sci. Technol., 49, 4646-4656, http://dx.doi.org/10.1021/es505577w, 2015.

Viana, M., Kuhlbusch, T. A., Querol, X., Alastuey, A., Harrison, R. M., Hopke, P. K., Winiwarter, W., Vallius, M., Szidat, S., and Prevot, A. S.: Source apportionment of particulate matter in Europe: A review of methods and results, J. Aerosol Sci., 39, 827-849, http://dx.doi.org/10.1016/j.jaerosci.2008.05.007, 2008.

Wang, F. W., Guo, Z. G., Lin, T., and Rose, N. L.: Seasonal variation of carbonaceous pollutants in $PM_{2.5}$ at an urban 'supersite' in Shanghai, China, Chemosphere, 146, 238-244, http://dx.doi.org/ 10.1016/j.chemosphere.2015.12.036, 2016.

Wang, J., Huang, J., Wang, L., Chen, C., Yang, D., Jin, M., Bai, C., and Song, Y.: Urban particulate matter triggers lung inflammation via the ROS-MAPK-NF-κB signaling pathway, J. Thorac. Dis., 9, 4398-4412, http://dx.doi.org/10.21037/jtd.2017.09.135, 2017.

Wang, N. L., Yao, T. D., Thompson, L. G., and Davis, M. E.: Indian monsoon and North Atlantic Oscillation signals reflected by $Cl^-$ and $Na^+$ in a shallow ice core from Dasuopu Glacier, Xixabangma, Himalaya, Ann. Glaciol., 273-277, https://doi.org/10.3189/172756402781816825, 2002.

Wang, Q. Z., Ding, H., Yu, F. W., Chao, N., Li, Y., Jiang, Q. Q., Huang, Y., Duan, L., Ji, Z. Q., Zhou, R., Yang, Z. P., Zheng, K. Y., and Miao, X. P.: The Characteristics and Impact Factors of Sulfate and Nitrate in Urban $PM_{2.5}$ over Typical Cities of Hangzhou Bay Area, China, Atmosphere, 14, http://dx.doi.org/10.3390/atmos14121799, 2023.

Weber, S., Uzu, G., Calas, A., Chevrier, F., Besombes, J. L., Charron, A., Salameh, D., Jezek, I., Mocnik, G., and Jaffrezo, J. L.: An apportionment method for the oxidative potential of atmospheric particulate matter sources: application to a one-year study in Chamonix, France, Atmos. Chem. Phys., 18, 9617-9629, http://dx.doi.org/10.5194/acp-18-9617-2018, 2018.

Xue, Y. H., Wu, J. H., Feng, Y. C., Dai, L., Bi, X. H., Li, X. A., Zhu, T., Tang, S. B., and Chen, M. F.: Source Characterization and Apportionment of $PM_{10}$ in Panzhihua, China, Aerosol Air Qual. Res., 10, 367-377, http://dx.doi.org/10.4209/aaqr.2010.01.0002, 2010.

https://doi.org/10.5194/egusphere-2025-626
Preprint. Discussion started: 20 May 2025
© Author(s) 2025. CC BY 4.0 License.

Yan, S., Diandou, X. U., and Zhifang, C.: Determination and characterization of anionic species of $PM_{10}$ and $PM_{2.5}$ in Beijing, Analytical Laboratory, 25, 80-85, http://dx.doi.org/10.3969/j.issn.1000-0720.2006.02.024, 2006.

Yang, G., Lee, H., and Lee, G.: A Hybrid Deep Learning Model to Forecast Particulate Matter Concentration Levels in Seoul, South Korea, Atmosphere, 11, http://dx.doi.org/10.3390/atmos11040348, 2020a.

Yang, L. I.: The space-time variations of $PM_{10}$ concentration in major cities of China during 2000-2007, Journal of Arid Land Resources and Environment, 23, 51-54, http://dx.doi.org/10. 13448/j. cnki. jalre. 2009. 09. 017, 2009.

Yang, L. M., Wang, S. B., Duan, S. G., Yan, Q. S., Jiang, N., Zhang, R. Q., and Li, S. L.: Characteristics and formation mechanisms of secondary inorganic ions in $PM_{2.5}$ during winter in a central city of China: Based on a high time resolution data, Atmos. Res., 233, http://dx.doi.org/10.1016/j.atmosres.2019.104696, 2020b.

Yao, K. X., Xu, Y. H., Zheng, H., Zhang, X. J., Song, Y. X., and Guo, H. B.: Oxidative potential associated with reactive oxygen species of size-resolved particles: The important role of the specific sources, J. Environ. Manage., 360, http://dx.doi.org/10.1016/j.jenvman.2024.121122, 2024.

Yu, D. J.,Wu, Y.L., Song, Q. L., Dai, X., Lin ,W.L.: Environmental Characteristics and Its Observations at Longfengshan WMO Regional Atmospheric Background Station, Climate Change Research Letters ,01, 65-73, http://dx.doi.org/10.12677/ccrl.2012.12008, 2012.

Yu, H., Zhao, X. Y., Wang, J., Yin, B. H., Geng, C. M., Wang, X. H., Gu, C., Huang, L. H., Yang, W., and Bai, Z. P.: Chemical characteristics of road dust $PM_{2.5}$ fraction in oasis cities at the margin of Tarim Basin, J. Environ. Sci., 95, 217-224, http://dx.doi.org/10.1016/j.jes.2020.03.030, 2020.

Yue, D. L., Zhong, L. J., Zhang, T., Shen, J., Zhou, Y., Zeng, L. M., Dong, H. B., and Ye, S. Q.: Pollution Properties of Water-Soluble Secondary Inorganic Ions in Atmospheric $PM_{2.5}$ in the Pearl River Delta Region, Aerosol Air Qual. Res., 15, 1737-1747, http://dx.doi.org/10.4209/aaqr.2014.12.0333, 2015.

Zhang, F., Wang, Z. W., Cheng, H. R., Lv, X. P., Gong, W., Wang, X. M., and Zhang, G.: Seasonal variations and chemical characteristics of $PM_{2.5}$ in Wuhan, central China, Sci. Total Environ., 518, 97-105, http://dx.doi.org/10.1016/j.scitotenv.2015.02.054, 2015.

Zhang, R., Cao, J., Tang, Y., Arimoto, R., Shen, Z., Wu, F., Han, Y., Wang, G., Zhang, J., and Li, G.: Elemental profiles and signatures of fugitive dusts from Chinese deserts, Sci. Total Environ. 472, 1121-1129, http://dx.doi.org/10.1016/j.scitotenv.2013.11.011, 2014a.

Zhang, T. T., Shao, Y., Gong, H. Z., Li, L., and Wang, L. F.: Salt Content Distribution and Paleoclimatic Significance of the Lop Nur "Ear" Feature: Results from Analysis of EO-1 Hyperion Imagery, Remote Sens., 6, 7783-7799, http://dx.doi.org/10.3390/rs6087783, 2014b.

Zhang, X. L. and Zhou, W. S.: Structural Vibration Data Anomaly Detection Based on Multiple Feature Information Using CNN-LSTM Model, Structural Control & Health Monitoring, 2023, http://dx.doi.org/10.1155/2023/3906180, 2023.

https://doi.org/10.5194/egusphere-2025-626
Preprint. Discussion started: 20 May 2025
© Author(s) 2025. CC BY 4.0 License.

Zhang, X. Y., Wang, Y. Q., Niu, T., Zhang, X. C., Gong, S. L., Zhang, Y. M., and Sun, J. Y.: Atmospheric aerosol compositions in China: spatial/temporal variability, chemical signature, regional haze distribution and comparisons with global aerosols, Atmos. Chem. Phys., 12, 779-799, http://dx.doi.org/10.5194/acp-12-779-2012, 2012.

Zhao, C. X., Wang, Y. Q., Wang, Y. J., Zhang, H. L., and Zhao, B. Q.: Temporal and Spatial Distribution of $PM_{2.5}$ and $PM_{10}$ Pollution Status and the Correlation of Particulate Matters and Meteorological Factors During Winter and Spring in Beijing,

Zhou, J., Elser, M., Huang, R. J., Krapf, M., Fröhlich, R., Bhattu, D., Stefenelli, G., Zotter, P., Bruns, E. A., Pieber, S. M., Ni, H. Y., Wang, Q. Y., Wang, Y. C., Zhou, Y. Q., Chen, C. Y., Xiao, M., Slowik, J. G., Brown, S., Cassagnes, L. E., Daellenbach, K. R., Nussbaumer, T., Geiser, M., Prevot, A. S. H., El-Haddad, I., Cao, J. J., Baltensperger, U., and Dommen, J.: Predominance of secondary organic aerosol to particle-bound reactive oxygen species activity in fine ambient aerosol, Atmos. Chem. Phys., 19, 14703-14720, http://dx.doi.org/10.5194/acp-19-14703-2019, 2019.